Thin Film Lasers Integrated with Planar Waveguides

A Dissertation
Presented to
The Academic Faculty
by
Hung-Fei Kuo

In Partial Fulfillment
of the Requirement for the degree
Doctor of Philosophy in Electrical and Computer Engineering

School of Electrical and Computer Engineering
Georgia Institute of Technology
August 2004

Thin Film Lasers Integrated with Planar Waveguides

Approved:

Dr. N. M. Jokerst, Chair

Dr. W. R. Callen, Jr.

Dr. G. K. Chang

Dr. A. B. Frazier

Dr. C. P. Wong

Date Approved: August 18, 2004

DEDICATION

This dissertation is dedicated to my parents, who believed in me and encouraged me on this long path.

ACKNOWLEDGEMENTS

I would like to express my appreciation to my thesis advisor, Dr. Nan Marie Jokerst, for her support throughout my Ph.D. experience. I would like to thank Dr. Gee-Kung Chang, Dr. W. Russell Callen, Jr. and Dr. A. Bruno Frazier for serving as my thesis reading committee members. I am also grateful to many colleagues, especially Mr. Yin-Jung Chang, Dr. Sang-Yeon Cho, Dr. Ye-Ming Li, and Dr. Shun-Der Wu for their assistance in my research work. Two of my very special friends, Ms. Carol Wu and Mr. Tweety Wu, I greatly appreciate for their support over during graduate school. Finally, I want to thank the members of my research group at Georgia Tech for their interactions related to my research.

TABLE OF CONTENTS

LIST OF FIGURES

LIST OF TABLES

SUMMARY

This dissertation describes the fabrication and integration of a thin film edge emitting laser (EEL) whose optical output is coupled into a polymer waveguide integrated onto the same electrical interconnection substrate. This embedded laser/waveguide structure is a fundamental building block toward the realization of planar lightwave circuits using embedded optical interconnections. The demonstration of a thin film laser integrated with a planar waveguide eliminates the need for either an external optical source coupled to the waveguide or a bump bonded optical source with a beam turning element to turn an optical beam into the waveguide. In this work, the wedge-induced facet cleaving (WFC) method is adapted to fabricate the thin film EELs. Bisbenzocyclobutene (BCB) polymers are used to fabricate channel waveguides, and thin film lasers are integrated with the polymer waveguides. The coupling efficiency from the laser to the polymer waveguide is estimated through measurement and theoretically calculated. In the theoretical calculation, the thin film transfer matrix method is used to analyze the optical modes in the semiconductor cavity. The coupling efficiency from the laser to the polymer waveguide is analyzed using a finite element method (FEM), and are then compared to the experimental results. The experimentally estimated coupling efficiency is in good agreement with that of the theoretical calculation. In addition, the relationship between threshold current, output power, and facet reflectivity of the thin film laser is analyzed using FEM.

CHAPTER 1

INTRODUCTION

Board and backplane-level interconnections are driving toward higher density interconnect and higher bandwidth. Many comparisons of interconnection performance have been published that discuss electrical and optical interconnections [1-3] The integration of optical interconnections into electrical interconnection backplanes and boards is a topic of currently intensive research. Optical interconnection approaches that are currently under investigation include free space interconnects with diffractive optical elements [4], silicon optical bench interconnects [5], and guided wave interconnections, including substrate guided mode interconnects [6], fiber optic waveguides [7], and integrated waveguides [8]. The research in this dissertation will focus upon guided wave optical interconnections, and explore the potential for fully embedded optical interconnections in which thin film lasers and polymer waveguides are integrated together onto SiO_2/Si substrates. Since these thin film lasers and waveguides are both on the order of microns thick, they can be integrated side by side in a series of microfabrication processing steps that create a planar lightwave integrated circuit on the surface of the substrate. Coupled with the recent results in the area of thin film optoelectronic device integration embedded in polymer waveguides integrated onto high temperature FR-4 printed wiring boards (PWBs) [9-11], this heterogeneous integration technology offers promising results for optical interconnections with lasers, waveguides, and photodetectors embedded in PWB for high performance optical interconnections integrated into standard electrical interconnection boards.

Currently, electrical interconnection systems are essentially planar, with perpendicular connections realized through wire bonded or bump bonded interposer substrates or vias. Thus, heterogeneously integrated planar waveguide optical interconnections match electrical systems from a planar topographical standpoint. If optically active devices, such as emitters and detectors, can be integrated into a system that can also host channel waveguides, a large "tool kit" of optical beam manipulation and optical function (splitters, wavelength division multiplexing (WDM) and spatial multiplexing) options can be implemented optically in the substrate plane. There are two basic approaches to the integration of optical signals into an electrical interconnection system at the backplane, board, and chip levels. The first utilizes surface normal optical beams that must be turned and coupled into the waveguide with a beam turning devices such as a mirror or a diffraction grating. These perpendicularly addressed optoelectronic emitters and detectors are usually bump bonded to the interconnection substrate with the optical emission or detection aperture facing the substrate. A commonly used emitter for this purpose is a Vertical Cavity Surface Emitting Laser (VCSEL), which emits from the top or bottom surface of the laser. VCSELs are particularly suited for coupling into optical fibers since the circular VCSEL output aperture can be designed to efficiently fill an optical fiber aperture. For bump bonded devices such as VCSELs and photodetectors, the air gap between the optoelectronic device and the board poses a packaging problem, in that it is risky not to encapsulate this gap. However, an underflow material must be optically transparent, not create additional optical loss with temperature and time, and not affect the alignment of the laser or photodetector to the beam coupler for launch into the waveguide. Finally, the underfill needs to be carefully co-designed with the beam coupler to ensure that the index of refraction of the underfill and the underfull/beam

coupler interface do not degrade the performance of the beam coupler. An alternative approach to integrated optical interconnections on electrical substrates confines the optical beam as a guided wave in the substrate, and utilizes thin film active optoelectronic devices bonded to the substrate that are integrated with planar channel waveguides. This approach can utilize external optical input/output signals, or the optical signals can originate and/or terminate in the waveguide directly on the board, without optical beam turning.

1.1 Hybrid Integration of Semiconductor Lasers with Optical Waveguides

The heterogeneous integration of semiconductor lasers and optical waveguides is a fundamental building block toward the realization of photonic integrated circuits (PICs) in an electrical interconnection format. A PIC is a system designed to have a certain function by integrating the lightwave components and electronic devices on a single substrate. The lightwave components can use lasers as optical sources and functional components, such as switches/modulators, interconnection waveguides, and photodiodes as detectors.

In PICs, semiconductor lasers are important light sources due to their narrow output spectrum, high efficiency, direct high-speed modulation, wide wavelength selectivity, and compact size. Semiconductor lasers are made of the III-V compound semiconductor material. In the field of fiber communication, Silica-based optical fiber has dispersion and absorption minima in the 1.3 μm and 1.5 μm regions, respectively, and semiconductor lasers have been optimized wavelength regions for these. There are two types of semiconductor lasers: EELs and VCSELs. The optical emission from an EEL is emitted into an elliptical cone and in a direction parallel to the active region of epilayer.

In contrast, VCSELs can produce a circularly symmetric beam in a direction perpendicular to the active region of epilayer. However, up to date, VCSELs appear to be limited to low output power in the longer wavelength ranges, 1.3 μm and 1.55 μm. [12-14].

The interconnections between lightwave components integrated in a PIC are low loss optical waveguides. There are many different forms of the optical waveguides, such as planar waveguides, optical fibers, or free space. For planar waveguides, they commonly consist of low loss dielectric materials, such as SiO_2 [15, 16], polymers [17, 18], for which the fabrication processes are simple, or III-V compound semiconductors [19, 20].

Methods for the integration of lightwave components in a PIC result in two types of structures: planar structures, and stacked structures. For the former one, the light signal propagates parallel to the integration substrate. The stacked structure differs from the planar type in that light propagates perpendicular to the integration substrate. PICs are very important functional blocks in contemporary optical interconnection areas, such as integrated distributed feedback (DFB) laser-electroabsorption modulators [21, 22], Y-junction power dividers [23, 24], wavelength division multiplexing (WDM) optical tranceiver chips [25-28], mode converters [29, 30].

1.2 Optical Interconnections

1.2.1 Background Concepts

The idea of using optical interconnections to solve electrical interconnection problems has been proposed by several researchers for its properties superior to conventional electrical interconnections. The important differences between optical and electrical interconnections are the carrier frequency, wavelength, and energy. Most of the benefits of optical interconnections come from these fundamental differences [3].

The carrier frequency of optical interconnections is very high compared with that of electrical interconnections. For example, a typical wavelength in optical communication systems is 1310 nm or 1550 nm, corresponding to around 230 THz. In typical microwave applications the carrier frequencies range from 300 MHz to 300 GHz. The high carrier frequency of optical systems results in negligible propagation loss and dispersive effects from large bandwidth signals at high frequency modulation. The dispersive effects of the optical systems only appear over large distances in fiber. Thus, there is no frequency-dependent loss or frequency-dependent cross talk when using light as a carrier between chips or between boards.

In optics, the wavelength of light is generally smaller than the dimensions of the dielectric optical waveguides. When optical waves are incident on a dielectric material, small oscillatory currents can flow the same way as polarizations of the electron clouds in the material. Such effects are strong enough to confine the optical waves in the dielectric waveguide. However, in the electrical case, waves are confined and directed over a small dimension in terms of the wavelength, from 0.1 cm to 1 m, in microwave applications. As a result, lossy conducting material is utilized to provide enough current response for the wave to guide. This results in high frequency-dependent loss because of the skin effect.

The fact that photon energy in optics is large leads to the result as follows. The light is generated and detected quantum mechanically. Specifically, the detection of light involves counting photons, not measuring the electric field amplitude, and the generation of light results from the recombination of an electron-hole pair. During the process of detection or generation, the photons have no memory of the current or voltage levels

within the electrical circuits. In other words, optical interconnections provide electrical isolation between two circuits.

The use of optical interconnections to improve local microelectronic systems can be in different level [31]: chip-level interconnections, multichip module (MCM) level interconnections, board level, and backplane interconnections. The chip-level interconnections are connections between devices on a very large-scale integrated (VLSI) circuit or chip. The MCM level interconnections are the connections between VLSI chips within a single MCM. The board level interconnections are connections between MCMs on a single printed circuit board.

The focus of this research is on board level optical interconnections. This type of technology includes the heterogeneous integration of optoelectronic components and complementary metal-oxide-semiconductor (CMOS) circuits. The optical emitter and the photodetector can be flip chip (bump bonded) to electrical processing circuitry in order to provide optical input-output (I/O) for VLSI integrated circuits as well as existing electrical I/O.

That is, long electrical interconnections can be replaced by an optical emitter, a photodetector, and interconnection optics between the optical emitters and photodetectors. Optical emitters can be light emitting diodes (LEDs), vertical cavity surface emitting lasers (VCSELs), and edge emitting lasers (EELs). The interconnection optics between optoelectronic components can be optical waveguides.

1.2.2 Schemes of Board Level Optical Interconnections

Several schemes of optical interconnections on board-level have been proposed [32-34]. These schemes can be divided into two categories based on the interconnection optics: free space optical interconnections and guided-wave optical interconnections. In the first category, as shown in Fig. 1, the light signal is emitted from a VCSEL transmitter array and redirected by the beam turning components. The beam turning components are composed of 45º mirrors and relay optics to reflect the optical signal from the VCSELs into the desired position on a photodetector array plane. In the middle of the optical path, collimating and focusing optics are employed to improve the beam quality and the alignment precision. In this type of architecture design, two issues are important: the optical alignment between each individual optical component, and the coupling loss between the optical components.

Figure 2 is an illustration of one type in the second category, a fully embedded board-level guided-wave optical interconnection [5]. Two types of schemes are introduced here. In the first scheme, as shown in Fig. 2, all elements involved in providing high-speed optical interconnections are embedded within one board. These include thin film

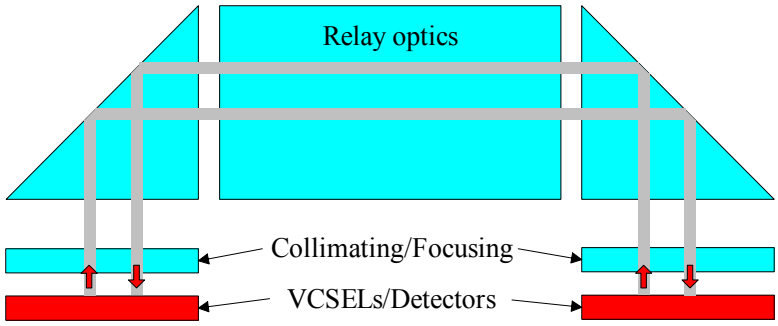

Figure 1. Optical interconnections using VCSELs through 45º mirrors, relay optics, and collimating/focusing optics.

VCSELs, surface-normal waveguide couplers, and thin film photodetectors. Polymer-based channel waveguides function as the physical layer of this optical bus. The optical signal is launched from a VCSEL and is totally reflected in a 45° waveguide coupler internally. This beam is redirected by another 45° waveguide coupler which turns the beam onto a detector. In this case, 45° waveguide couplers are made of slanted gratings, which are very difficult to fabricate. Moreover, the mismatch loss between the circular VCSEL mode and the planar channel waveguide mode is also an issue.

In the second scheme of the fully-embedded board-level guided-wave optical interconnection, as shown in Fig. 3**,** a metal semiconductor metal (MSM) photodetector is embedded inside the waveguide core or cladding on top of an electrical interconnection substrate [35]. The beam in the optical fiber is coupled into the planar channel waveguide by the end facet coupling method. The light signal travels in the channel waveguide and then is detected by the MSM photodetector through evanescent coupling method. The coupling loss from the optical fiber to the channel waveguide can be high. The coupling loss is caused by several factors, such as, the waveguide entrance facet quality, the mismatch between the fiber mode shape and the channel waveguide mode

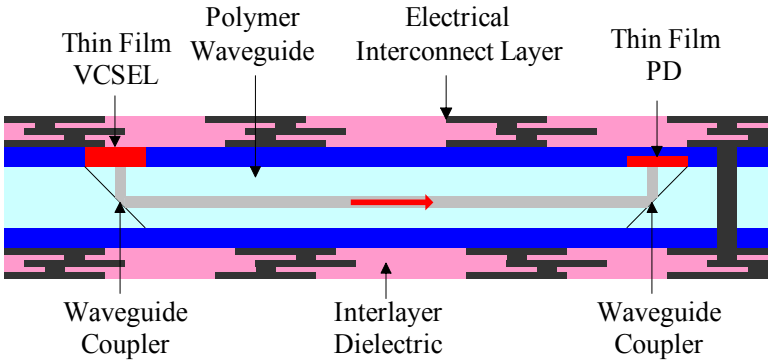

Figure 2. Optical interconnections using VCSELs through 45º waveguide couplers and a polymer waveguide.

shape, and the optical axis misalignment between the fiber and the waveguide. On the other hand, if EELs are integrated on the substrate with the planar waveguide, efficient power coupling could be achieved with simplified optical system design. The EELs would also result in a matched transverse mode pattern.

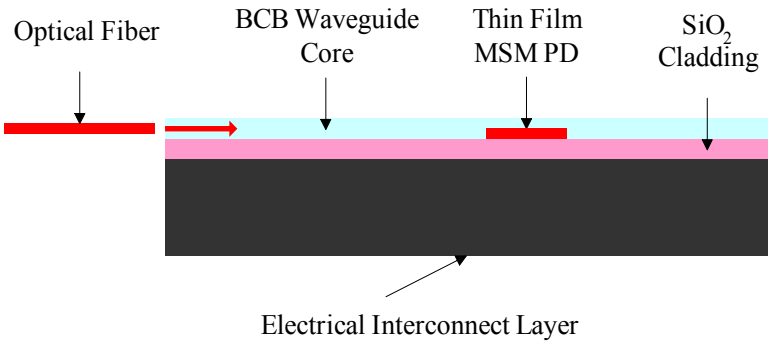

Figure 3. Optical interconnections using an optical fiber and a thin film MSM photodetector.

1.3 Fabrication of Thin Film EELs

The fabrication of thin film edge emitting lasers has been reported in [36-38]. In [36], the epitaxial InP/InGaAsP wafer is bonded to a glass plate for mechanical support. Utilizing an InGaAs stop etch layer, the InP substrate is selectively removed to leave a thin epitaxial film on the glass plate. This thin epitaxial film is transferred and then bonded to a Si substrate at 400 ºC for 30 minutes. After bonding, an 8 µm wide mesa stripe is formed using wet chemical etching. The active layer is slightly undercut to reduce the active width. Finally, Ni/AuGe and AuZn are evaporated and alloyed at 400ºC to form n-type and p-contact ohmic contacts, respectively. After thinning the Si substrate down to about 100 µm, the fabricated lasers are then cleaved into different cavity lengths and tested. The threshold current density and the external quantum efficiency of these lasers are 2 kA/cm^2 and 25%, respectively, for a 300 µm long cavity.

In [37], the lasers are 980 nm InGaAs/GaAs strained single quantum well lasers with a graded-index separate confinement heterostructure (GRINSCH). In addition, a n-AlAs sacrifical layer with thickness 1000 Å is grown between the laser structure and GaAs substrate. Conventional ridge waveguide laser structures with 5 μm width are preprocessed. The preprocessed laser diodes on the GaAs substrate are covered with black wax on top and soaked in 10% HF solution to selectively remove the AlAs layer. This epitaxial layer, after separation from the GaAs substrate, is dipped in HCl and HF before the bonding process. A n^+ Si substrate is used as the host substrate in this process. A Pd/Ge/Pd metallic multilayer is deposited on the Si substrate. After deposition, the Si substrate is lapped down to 100 μm, and an Al film is evaporated onto the backside as an ohmic contact. Finally, the thin film and the n^+ Si substrate are bonded together by Van Der Waals bonding. The bonded sample is heated in a furnace at 400 ºC for 30 minutes under a forming gas ambient. The final device thickness is around 100 μm. The threshold current and the slope efficiency of these lasers are 16.3 mA and 0.4 mW/mA, respectively, for a cavity length of 800 μm.

In [38], a broad area contact is first defined on the top GaAs contact layer. Apizeon wax is then deposited on the preprocessed surface and HF: H_2O is used to laterally etch the AlGaAs layer which is grown between the epilayers of interest and the growth substrate. An Au/Ge-Ni ohmic n-type contact is deposited after epitaxial separation on the released side. Trichlorethylene (TCE) is then used to remove the Apizeon wax and the thin film EEL is attached to a wax-coated intermediate GaAs substrate for wedge-induced facet cleaving (WFC) processing. Wedge patterns are first defined in the photoresist on the epitaxial surface and are then etched down to the substrate. Next, the thin film EELs are released from the GaAs carriers and attached to a thin metal using

Apizeon wax. By bending this flexible carrier, cleaves along the (011) plane are induced along each wedge. Finally, these cleaved lasers are detached from the carrier and mounted on the edge of a Si substrate with a 2 μm layer of In. When the devices are tested, the threshold current density and the external quantum efficiency of these lasers are 640 A/cm^2 and 15%, respectively, for a 250 μm long cavity.

For the method used in [36], it is difficult to align the InP and Si crystal directions. For the method used in [36] and [37], the 100 μm final device thickness also prevents the integration of these thin lasers with waveguides. However, for the method used in [38], the WFC lasers can be embedded in a waveguide. Using the WFC cleaving method, the lasers could have a shorter cavity length than the 200 ~ 300 μm length demonstrated in [13]. A problem associated with the WFC method is the curvature of the thin films. After the epilayers are detached from the growth substrate, stress can cause the thin film devices to deform. Generally, this stress can be divided into compressive stress and tensile stress, as shown in Fig. 4. In both cases, it is difficult to bond the thin film lasers and integrate them with optoelectronic components. Moreover, the light propagates along the curved optical path in the laser, resulting in an increase in optical power leaking out of the waveguide core region. This is detrimental to laser performance, or it results in a higher threshold current and a lower power output.

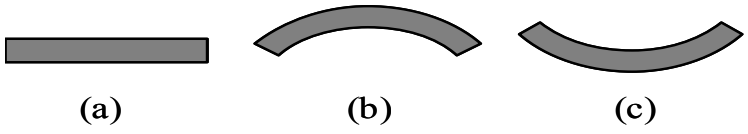

Figure 4. Thin film stress: (a) unstressed; (b) with compressive stress; and (c) with tensile stress.

1.4 Research Objectives

Board-level interconnections are driving toward higher density interconnect and higher bandwidth. Optical interconnections are one board-level technology that can address these issues in a System on a Package (SOP) format. An interesting approach to SOP optical interconnections is to embed the optical interconnections in the package in a post-processing format. In spite of recent progress in this field, most of these approaches embed the active optical elements (emitters, detectors) in the host interconnection substrates which must then be Si or GaAs. This dissertation is the first demonstration of a thin film MQW InGaAsP/InP EEL bonded onto an interconnection substrate where the laser optical output is coupled into a waveguide integrated on the same substrate. This embedded laser/waveguide structure is a fundamental building block toward the realization of planar lightwave circuits with embedded optical interconnections. The contributions of this research are organized in different areas as listed below.

1. The use of VCSELs is popular for the fiber optic coupling due to the circularly symmetric surface normal output characteristic. They are excellent candidates for applications to free space, unit level, or cabinet level optical interconnections. However, in a planar waveguide format, EELs are better candidates. The emitted light coupled out of EELs is parallel to the integration substrate plane, which no longer requires the beam turning elements to turn the beam on/out of the plane nor requires the optical components in the middle of the optical path to collimate the optical beams. In this dissertation, both of the design and fabrication method of the optical interconnection with thin film InGaAsP/InP MQW EELs are presented.

2. In a ligthwave system, the alignment between optical components is a key issue to optimize the optical power budget and to control packaging cost. In this research work, the developed thin film InGaAsP/InP EELs can be heterogeneously integrated onto the interconnection substrate with subsequent deposition of the waveguide onto the lasers since the lasers are in the order of microns thick. The alignment between EELs and the optical waveguide is completed through photolithographic masking steps, which is a cost effective method. This dissertation presents the first integration of thin film lasers with polymer waveguides.
3. The use of VCSELs coupled to fiber is preferred due to the mode matching of the circular VCSEL to the fiber core. However, the mode patterns for the VCSELs are different from the elliptical mode patterns for the channel waveguides. When the light coupled out of the VCSELs is emitted into channel waveguides, the mode pattern dissimilarity between these two devices causes mode mismatch loss. The mode mismatch loss for the EELs is less than that of the VCSELs since the mode patterns for the EELs are elliptical in shape due to the planar format waveguide of the EEL Fabry-Perot resonator. In this dissertation, the analysis of coupling efficiency from the thin film EELs to the polymer channel waveguides is presented.
4. In order to make electronic systems with integrated optical interconnections compatible with long haul optical network, optical sources with long wavelengths at 1.3 μm or 1.5 μm regions are desired. Low optical power output in these wavelength regions makes the VCSELs less suitable for these applications. However, EELs have been developed, and are mature, with high output power in

these wavelength regions. This dissertation furthers the development of the conventional MQW EELs into the first thin film (less than 10 μm thick) MQW InGaAsP/InP EEL.

The material explored in this research is in the InGaAsP/InP material system. However, the fabrication method developed in this dissertation is not limited to this material system.

1.5 Dissertation Overview

This dissertation presents the first thin film (less than 10 μm thick) InGaAsP/InP MQW lasers and the first integration of the thin film lasers with planar channel polymer waveguides. In Chapter 2, the fundamental principles of thin film InGaAsP/InP gain-guided EELs are reviewed. The chapter begins by introducing the electrical and optical confinement in the gain-guided structure. Optical gain in the unstrained MQW regions and lasing conditions for the gain-guided lasers are also addressed. The measurement of the laser performance, such as threshold current and power output, is discussed in detail. The principles of waveguide modes in BCB polymer waveguides and the BCB polymer properties are also presented. The end facet coupling from the lasers to the waveguides will also be reviewed. The chapter concludes with the use of FEMs to analyze the coupling efficiency from the lasers to the waveguides.

Chapter 3 contains the basic guidelines on the design and fabrication of thin film InGaAsP/InP gain-guided EELs and BCB polymer waveguides. The integration of the lasers and the waveguides is presented in detail. Results obtained from the testing of thin film edge emitting lasers and the integrated structures are also presented. Key issues related to the design, fabrication, and integration of the laser and the waveguide are discussed at the end of Chapter 3.

Chapter 4 is focused on the theoretical analysis of the integration structure. The transfer matrix method is applied to the multilayer semiconductor waveguides for the analysis of waveguide modes. Next, the existing transverse mode functions are inserted into commercial FEMs software, FEMLAB, to complete the analysis of coupling efficiency from the laser to the waveguide as a function of separation between the devices. The facet reflectivity of the embedded lasers and its effect on the threshold current and output power will be discussed. At the end of Chapter 4, the output power as a function of separation between the lasers and the waveguides using both results from the experiments and those obtained via theory are compared. The dissertation ends with Chapter 5 by summarizing the contributions of the dissertation work and outlining directions for future work.

CHAPTER 2

THIN FILM INGAASP/INP EELS and PLANAR BCB WAVEGUIDES

2.1 Introduction

The fundamental configuration of EELs is composed of active layers, which are InGaAsP/InP material system in this research, and a pair of mirrors, which are usually cleaved facets perpendicular to the active layer. The most important part of the EELs is its active layer. In this research, InGaAsP MQWs are chosen for the active layers since the density of states is lower than that of the conventional bulk materials. The EELs are typical pn-junction devices. The operating mechanisms of the EELs are based on the electrical and optical properties of pn junctions and semiconductor materials. For the electrical properties, under the forward bias condition, the minority carriers are injected into the active layer through the pn junction while the majority carriers diffuse into the active layer. The coherent light from the stimulated emission process in the active layer is emitted from the cleaved facets in opposite directions. The confinement of photons in the EELs can be accomplished by setting the refractive index of the active layer higher than that of the cladding layers. Emitted light propagates along the high refractive index region. The combination of InGaAsP and InP is a typical example of pairs of materials with appropriately related refractive indexes. The refractive index of InGaAsP active layers is a few percent higher than that of InP cladding layers. The emitted light is thus confined to the active layer. Based on the confinement of transverse optical modes, EELs can be divided into two different groups: gain-guided and index-guided lasers. In this research, gain-guided InGaAsP/InP lasers are used.

2.2 Thin film Gain-Guided Lasers

2.2.1 Electrical and Optical Confinement

Gain-guided EELs, which have stripe contacts on the p-side and broad contacts on the n-side, are simple lasers to fabricate and have been commercially available for over 20 years, and are illustrated in Fig. 5 [39]. Many interesting physical characteristics can be extracted from these lasers, including the optical gain, threshold current, and optical power output.

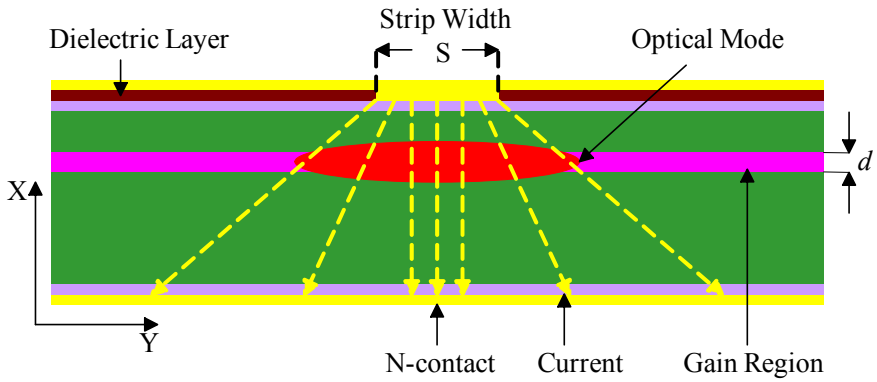

Figure 5. Structure of a gain-guided laser.

In gain-guided lasers, dielectric layers are used for current confinement within the gain-guided structures. Current is injected into the opening of the dielectric layers, stripe width S (typically, 10 to 50 μm wide stripes). The thickness of the active layer is d. The injected current density, $J(y)$, can be represented as

$$J(y) = \begin{cases} J_0 & |y| \le S/2 \\ J_0 \exp[-K(|y| - S/2)] & |y| \ge S/2 \end{cases} \quad (1)$$

where K accounts for the current spreading [40-42]. The injected current J spreads along the lateral direction. If the current spreading outside of the stripe region is ignored, the carrier distribution, $n(y)$, is represented as

$$n(y) = N_0 \begin{cases} \left(1 - \exp\left[-\frac{S}{2L_n}\right] \mathrm{Cosh}\left[\frac{y}{L_n}\right]\right) & |y| \le S/2 \\ \mathrm{Sinh}\left[\frac{S}{2L_n}\right] \exp\left[-\frac{|y|}{L_n}\right] & |y| \ge S/2 \end{cases} \quad (2)$$

where L_n is the diffusion length and N_0 is the carrier distribution at the thermal equilibrium [43,44].

Therefore, the carrier density n distributes along the Y direction, as determined by the current spreading and the lateral current diffusion. The effective width of the carrier density distribution and the gain profile along the lateral direction are wider than the strip width S. The current density profile and the carrier density profile are shown in Fig. 6.

Light amplification due to stimulate emission occurs only in the gain region under the stripe in an area defined by the current spreading from the stripe. Under high injection conditions, the carrier density of the central light-emitting region decreases because of the high rate of stimulated emission. This reduction of the injected carrier density leads

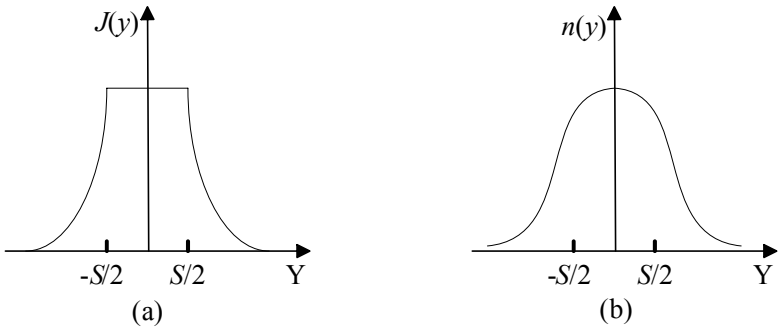

Figure 6. (a) Distribution of the current density; (b) Distribution of the carrier density.

to an increase in the refractive index. This difference between the refractive index inside and outside of the gain region causes the transverse optical modes to be confined within the center of the MQW region in the Y direction.

Confinement of the transverse optical modes along the X direction is then achieved by the use of heterostructures such as $In_{1-x}Ga_xAs_yP_{1-y}$. When the percentage of arsenic (x) increases, the band gap energy decreases and the refractive index increases. The analytic forms of parameters [45] for the case of $In_{1-x}Ga_xAs_yP_{1-y}$ lattice-matched to InP (for which $x \approx 0.45y$) are in Table 1. With confinement along both the X and Y directions, the optical modes maintain their relative shape while propagating along the Z direction.

Table 1. Summary of band structure parameters of $In_{1-x}Ga_xAs_yP_{1-y}$ lattice-matched to InP.

Parameter	Dependence on the mole fractions x and y
Energy gap at undoped	Eg (in eV) = $1.35-0.72y+0.12y^2$
Refractive index	$3.4+0.256y-0.095y^2$
Heavy-hole mass	$m_{hh}/m_0 = (1-y)[0.79x+0.45(1-x)]+y[0.45x+0.4(1-x)]$
Light-hole mass	$m_{hh}/m_0 = (1-y)[0.14x+0.12(1-x)]+y[0.082x+0.026(1-x)]$
Spin-orbit splitting	Δ (in eV)= $0.11+0.31y-0.09y^2$
Conduction-band mass	$m_e/m_0 = 0.08-0.39y$

The propagating fields in the MQW active region (see Fig. 5) are separated into two independent sets: transverse electric (TE) modes and transverse magnetic (TM) modes. The optical electric field is in the Y direction for TE modes and lies in the XZ plane for the TM orientation. Most of the gain-guided lasers oscillate in the TE modes because the reflectivity of the cleaved facets for this polarization is higher than for the TM case. The facet reflectivity of the TE modes for InP/InGaAsP gain-guided lasers is about 30% [46].

2.2.2 Optical Gain in Unstrained MQW Regions

In this dissertation, unstrained MQW epilayers act as the gain region for stripe contact edge emitting lasers. The energy bands in MQW semiconductor materials result from the periodic structure of the lattice. When the crystal thickness is finite and thin enough to be comparable to the de Broglie wavelength of an electron in a semiconductor (≈ 10 nm), the energy levels become discrete, as shown in Fig. 7. Along the X direction in Fig. 5, electrons are confined by the potential well made by the hetero-structures, which results in quantized energy levels. Along the Y and Z directions in Fig. 5 (parallel to the interface of the heterojunctions), the crystal is assumed to be infinite. The density of states of electrons and holes forms a step-like function in the quantum well region in such a structure. This results in the electron distribution and hole distribution being different from those of conventional bulk materials. Due to this effect, low threshold current and high slope efficiency can be obtained [47].

Not all of the states in the conduction bands and valence bands can participate in the optical transition. The spin of the state must also be conserved. The conservation of

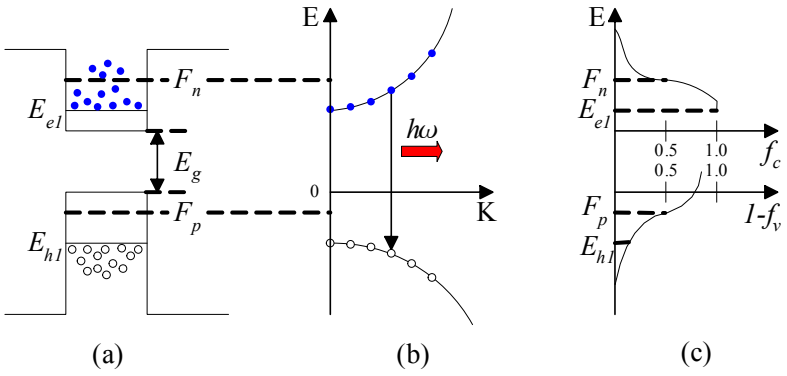

Figure 7. (a)The energy profile in real space; (b)The energy dispersion in real space; (c) The Fermi-Dirac function vs. the energy for the electrons in conduction band and for the holes in the valence band.

momentum, $\hbar k$, puts an additional restriction on the number of states available. The reduced density of states of the electrons and holes are thus described by

$$\rho_{2D} = \frac{m_r}{\pi\hbar^2 L_x} H(\hbar\omega - E_{nm}) \tag{3}$$

where $\hbar$ is the Planck constant h divided by 2π, m_r is the reduced mass, L_x is the width of the quantum well, H is the Heaviside step function, ω is the angular frequency, and Enm is the band edge transition energy, which is $E_g + E_{en} - E_{hm}$.

Under current injection, a significant number of excess electrons and holes are injected into the conduction band and valence band. Since this current injection is strong enough to force the semiconductor system to deviate far away from thermodynamic equilibrium, a quasi-Fermi level F_n is required to describe the probability of a state being filled with an electron in the conduction band, and F_p is required to describe the probability that a state in the valence band is filled with a hole. At thermal equilibrium, $F_n = F_p = E_f$, which is the Fermi-level. The probabilities of an occupied state in the conduction band $f_c(E)$ and in the valence band $f_v(E)$ are

$$f_c(E) = \frac{1}{exp[(E - F_n)/kT] + 1} \tag{4}$$

$$f_v(E) = \frac{1}{exp[(E - F_p)/kT] + 1} \tag{5}$$

where k is the Boltzmann constant, T is the temperature and E is the energy of the state.

When an optical wave with photon energy $hv > E_g + E_{e1} - E_{h1}$ passes through the MQW region, electrons are promoted from filled states in the valence band to empty states in the conduction band. This process is known as absorption. At the same time,

the wave can stimulate optical emission, and electrons in the conduction band emit and fall to the empty states in the valence band. This process is known as stimulated emission. When the stimulated emission rate exceeds the absorption rate, the optical wave experiences gain in the MQW region. The gain coefficient in a quantum well can be described as [48]

$$g(\hbar\omega) = \frac{\pi e^2}{n_r c \epsilon_0 m_0^2 \omega} \sum_{n,m} |I_{nm}|^2 |\hat{e} \bullet \boldsymbol{p}_{cv}|^2 [f_c(E_{en}) - f_v(E_{hm})] \rho_{2D} \qquad (6)$$

where ω is the photon radial frequency, n_r is the refractive index, ϵ_0 is the permittivity of free space, e is the electronic charge, m_0 is the electron rest mass, c is the speed of the light in vacuum, I_{nm} is the overlap integral of the conduction band and valence band envelope function, f_c and f_v are the Fermi distribution functions for the conduction band and valence band, ρ_{2D} is the reduced density of states, and $\boldsymbol{p}_{cv}$ is the momentum matrix.

In Eq. 6, the term $f_c(E_{en}) - f_v(E_{hm})$ must be positive in order for there to be optical gain. It occurs only at $E_g + E_{en} - E_{hm} < h\nu < F_n - F_p$, which is the condition to reach population inversion in a quantum well region in gain-guided lasers. The other parameter, $\boldsymbol{p}_{cv}$, the momentum matrix elements, is summarized in Table 2 [49]. In Table 2, $\mathbf{M}_{c\text{-}hh}$ represents the optical transition from the conduction band to the heavy hole band, and $\mathbf{M}_{c\text{-}lh}$ represents the optical transition from the conduction band to the light hole band. From Table 2, it is obvious that TE and TM polarized optical waves experience different gains in laser materials. For unstrained MQW lasers, the gain for the TE polarization is larger than that for the TM polarization since most of the holes occupy the heavy hole subbands.

Table 2. Summary of the momentum matrix elements in the parabolic band model ($|e\, p_{cv}|^2 = |e\, M|^2$).

TE polarization $(\hat{e} = \hat{x} \text{ or } \hat{y})$	**TM polarization** $(\hat{e} = \hat{z})$
$\langle \mid \hat{e} \cdot \mathbf{M}_{c\text{-}hh} \mid^2 \rangle = \frac{3}{4} (1 + \cos^2\theta) M_b^2$	$\langle \mid \hat{e} \cdot \mathbf{M}_{c\text{-}hh} \mid^2 \rangle = \frac{3}{2} \sin^2\theta\, M_b^2$
$\langle \mid \hat{e} \cdot \mathbf{M}_{c\text{-}lh} \mid^2 \rangle = \left(\frac{5}{4} - \frac{3}{4} \cos^2\theta\right) M_b^2$	$\langle \mid \hat{e} \cdot \mathbf{M}_{c\text{-}lh} \mid^2 \rangle = \frac{1}{2} (1 + 3\cos^2\theta) M_b^2$
$M_b^2 = \left(\frac{m_0}{m_e^*} - 1\right) \frac{m_0 E_g (E_g + \Delta)}{6 (E_g + \Delta)}$	

2.2.3 Threshold Current and Output Power

Threshold current and output power are two important parameters for semiconductor lasers. They are performance characteristics determined by the basic properties of the materials and structures used for the lasers. Basically, the threshold current is defined by the lasing conditions. The optical output power is expressed using the external quantum efficiency and the threshold current.

The lasing conditions for an optical cavity formed by an active layer with length L, and two mirror facets of reflectivity, R_1 and R_2, are given by [39]

$$g_{th} = \alpha_i + \left(\frac{1}{L}\right) \ln\left(\frac{1}{R}\right), \quad R = R_1 R_2 \tag{7}$$

$$m\left(\frac{\lambda_0}{n_r}\right) = 2L \quad (m = 1, 2, 3, \ldots) \tag{8}$$

where g_{th} is the gain coefficient at threshold, α_i is the total internal loss, m is the mode index, λ_0 is the optical wavelength in free space, and n_r is the effective refractive index in

the guiding layer. The first lasing condition, Eq. 7, relates the threshold gain to the loss. The threshold current can be described by [50]

$$J_{th} = d\left(\frac{g_{th}}{g_0 \Gamma_a} + J_0\right) \tag{9}$$

where g_0 is the gain constant, d is the active layer thickness, Γ_a is the optical confinement factor, and J_0 is the transparency current density. The threshold current density is an important basic parameter for gain-guided lasers. It is a performance measure determined by several factors, such as, optical gain, mirror loss, scattering loss, and cavity loss. The mirror loss is caused by the mirror facet reflectivity being less than 100%. The scattering loss is caused by structural inhomogeneities such as the roughness of the heterointerface. The cavity loss is primarily attributed to the absorption loss.

The second lasing condition, Eq. 8, determines the emission spectrum which is closely related to lasing. Lasing occurs at the wavelength mode satisfying Eq. 8. The lasing modes are determined by the light propagating in the direction of the laser cavity and are called the longitudinal modes or axial modes. The full-width at half-maximum of an envelope of the longitudinal mode often exceeds a few nanometers. Before lasing, the envelope is quite broad, but it becomes narrow after lasing because only the modes near the maximum gain can lase.

The behavior of gain-guided laser diodes is quite similar to LEDs before lasing, and the spontaneous emission power is emitted from both facets. The output power efficiency is quite low at this stage. When the injected current is greater than the threshold current, stimulated emission exceeds spontaneous emission, and the output power efficiency increases quickly. The output power after lasing is usually expressed by using the external quantum efficiency and threshold current as

$$P_{out} = \left(\frac{1}{2}\right) h\nu\eta_d \frac{[I_F - I_{th}]}{q} \tag{10}$$

where η_d is the external quantum efficiency and I_f and I_{th} are the forward injected current and the threshold current, respectively.

2.3 Planar Optical Waveguides

2.3.1 Optical Modes in Planar Waveguides

In this research, the 3000 series of dry-etch BCB resins are used as the waveguide core material. These BCB polymers, made by the Dow Chemical Company, have been developed for use in microelectronics applications. Due to their excellent properties, including high level of planarization, high optical transparency, low cure temperature (<200 ºC for 4 hours curing), high solvent resistance, and low moisture uptake, they are very attractive for application in the field of optoelectronics. The optical properties of the BCB materials used in this research are summarized and listed in Table 3 [51-55]

Table 3. CYCLOTENE 3022-46 BCB properties.

Physical properties	Frequency/Wavelength ranges
Dielectric constant ϵ_r: 2.65	1 ~ 10 GHz
Dissipation factor Tan δ: 0.0008 ~ 0.0002	1 MHz ~ 10 GHz
Volume resistivity 1×10^{19} ohm-cm	Tensile strength: 87 MPa
Moisture uptake	Tensile modulus: 2.9 GPa
Loss: 0.4 dB	1310 nm
Refractive index: 1.52	1310 nm

Thin film BCB deposited on a dielectric substrate can be used as an optical waveguide if the refractive index of the BCB is higher than that of the substrate. A basic step index waveguide structure is shown in Fig. 8, with the refractive index profiles along the depth, where the indices of the cladding layer, waveguide core layer, and substrate are

n_c, n_f, and n_s, respectively. The θ in Fig. 8 is defined as the angle between the wave normal and the normal to the interface in the step index waveguide. The waveguide illustrated in Fig. 8 is a 2-D optical waveguide (or a slab optical waveguide) because light confinement takes place only in the X direction.

For the step index waveguide using a ray tracing approximation, the critical angles at both upper and lower interfaces are $\theta_c = \sin^{-1}(n_c/n_f)$ and $\theta_s = \sin^{-1}(n_s/n_f)$, respectively. Since $n_s > n_c = 1$, $\theta_s > \theta_c$. On the basis of these two critical angles, three types of modes propagate in the optical waveguide: (1) a guided mode; (2) a substrate mode; and (3) a radiation mode, as shown in Fig. 9. For the guided mode, $\theta_s < \theta < 90°$, and the light is confined in the guiding layer by total internal reflection at both the upper and lower interfaces. The light can propagate without attenuation if the waveguide material is lossless.

If $\theta_c < \theta < \theta_s$, the light is totally reflected at the upper interface while it leaks out of the waveguide core layer through the cover. This light is in substrate mode operation,

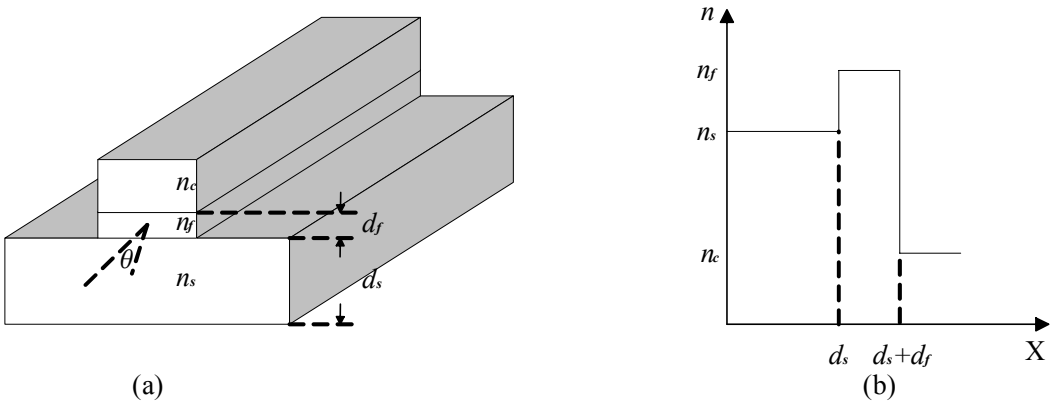

Figure 8. (a) Step index waveguide structure; (b) Refractive index profile.

and the optical amplitude decreases significantly along the propagation direction. The $\theta < \theta_c$ condition leads to a radiation mode that radiates to both the cover and the substrate. The relationship between the incident angle θ and the propagation constants along the X and Z directions are $k_x = k_0 n_f \cos\theta$ and $\beta = k_0 n_f \sin\theta$ in a lossless waveguide [56]. The effective indices N of guided modes can be defined as $\beta = k_0 N$ where $N = n_f \sin\theta$ [56].

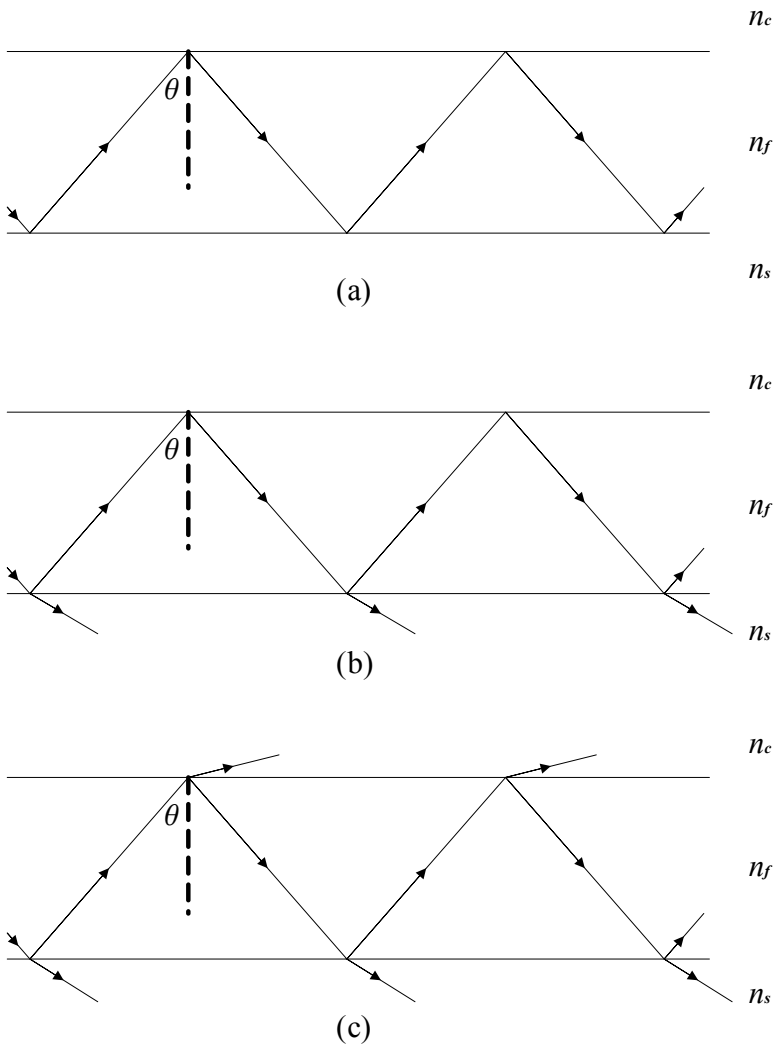

Figure 9. (a) Guided mode $\theta_s < \theta < 90°$; (b) Substrate mode $\theta_c < \theta < \theta_s$; (c) Substrate and radiation modes $\theta < \theta_c$.

2.3.2 Coupling from the Thin Film Lasers to the Waveguides

There are several methods for the excitation of a guided wave in the polymer waveguide, such as the end-facet coupling method, the prism coupling method, and the grating coupling method. In the end-facet coupling method, light can be coupled from a laser to an optical waveguide via the use of microlenses [57], spot size converters (SSC) [58], or simple endfire coupling.

When a microlens is used, the typical coupling efficiency from the laser to the fiber is 70% [59]. The microlens studied is created through the deposition of SiO_2 on the emitting surface of a laser diode. The microlens can be formed as an elliptical, spherical, or aspherical shape to collimate or focus the laser beam directly from the emitting surface. When spot size converters are used, the coupling efficiency can be raised to 75% from a spot-sized converted laser diode to a silica waveguide [60]. The SSC laser diodes (SSC-LDs) are composed of both an active and a passive waveguide. The active waveguide is tapered to transfer the optical power into the passive waveguide. The mode profile is determined by the well-defined passive waveguide. In both cases, lower loss and higher alignment tolerance of the laser input to planar waveguides can be achieved by adding extra optical components.

In this research work, the end-facet coupling method is used for guided-wave excitation, as shown in Fig. 10. End-facet coupling is the simplest way to couple light from optical sources to waveguides. The coupling efficiency between EELs and the optical waveguides depends on alignment, dimensional differences, and geometric shape. In Fig. 10, the cleaved end facet of the EEL is butted up against the polymer waveguide with separation distance, d. The thickness of the thin film EEL, the thin film polymer waveguide, and the integration substrate are t_l, t_f, and t_s, respectively. The refractive

index of the polymer film and the integration substrate are n_f, and n_s, respectively. For optical mode operation designed in this dissertation, the thickness of the guided layer, t_f, is 5 μm. The fundamental guided-mode profile is close to a Gaussian spatial shape. In order to obtain high efficiency coupling from the laser to the waveguide, the incident wave profile has to be as close as possible to the profile of the mode to be excited. The divergence of the input beam should not exceed the acceptance angle, θ_{max}, determined by the numerical aperture (NA), $\sqrt{(n_f^2 - n_s^2)}$, of the waveguide [56]. The θ_{max} is given as a function of NA: $n_c \sin^{-1} NA$. Light incidents at an angle larger than the θ_{max} leaks out to the substrate.

With the use of BCB polymer waveguides, the distance, d, is controllable from 0 to 15 μm using photolithography and dry etching methods. By defining the waveguide channel, the inherent accuracy of the photolithographic processing reduces the possibility of misalignment between the EEL and the polymer waveguide.

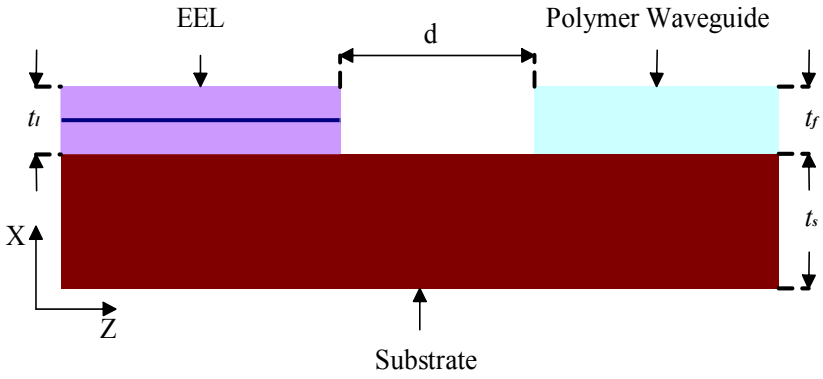

Figure 10. Guided wave excitation by end facet coupling.

2.4 Simulation of Thin Film Lasers and Planar Waveguides

2.4.1 Static Properties of Thin Film Lasers

In order to design the MQW InGaAsP/InP lasers, a computer aided design (CAD) tool, the Laser module in Silvaco (commercial software), was employed to perform the analysis in this research work. The Laser module solves the Helmholtz equation to calculate the optical field and photon densities. Several important parameters for the semiconductor lasers can also be calculated, including the carrier recombination due to light emission, the optical gain dependence on the photon energy and the quasi Fermi level, the light intensity profile corresponding to the fundamental mode, and the modal gain spectra for several longitudinal modes. The fundamental semiconductor equations, Eq. 11, Eq. 12, and Eq. 13, are solved self-consistently with a two dimensional Helmholtz equation, Eq. 14, for the local optical gain calculation. Poisson's equation is used, which relates the electrostatic potential to the space charge density,

$$\nabla \cdot (\epsilon \nabla \varphi) = -\rho_c \tag{11}$$

where φ is the electrostatic potential, ϵ is the local permittivity, and ρ_c is the local space charge density [39]. The electrical field, E, is obtained from the gradient of the potentional [39].

$$\frac{\partial n}{\partial t} = \frac{1}{q} \nabla \cdot \vec{J}_n + G_n - R_n \tag{12}$$

$$\frac{\partial p}{\partial t} = \frac{1}{q} \nabla \cdot \vec{J}_p + G_p - R_p \tag{13}$$

Eq. 12 and Eq. 13 are the continuity equations for electrons and holes, respectively, where n and p are the electron and hole concentrations, J_n and J_p are the electron and hole current densities, G_n and G_p are the generation rates for electrons and holes, R_n and R_p are the recombination rates for electrons and holes, and q is the magnitude of the charge on an electron.

Equation 14 is a complex eigenvalue equation [61]. There are the set of complex eigenvalues β_k and corresponding eigenfunctions $E_k(x,y)$ in Eq. 14. The fundamental transverse mode is only taken into account only in the simulations. Therefore, the index k will be dropped from subsequent equations.

$$\nabla_{xy}^2 E_k(x, y) + \left(\frac{\omega_m^2}{c^2} \in (x, y) - \beta_k^2 \right) E_k(x, y) = 0 \tag{14}$$

For dielectric permittivity $\epsilon(x,y)$, the following model is used [61]:

$$\in (x, y) = n_0^2 + (-\alpha_r + j) \frac{n_0 \, g(x, y)}{k_\omega} - j \frac{n_0 (\alpha_a + FCN \cdot n + FCP \cdot p)}{k_\omega} \tag{15}$$

where n_0 is the bulk refractive index, α_r is a line width broadening factor, and j is $\sqrt{-1}$, k_ω is ω/c, g(x,y) is the local optical gain, α_a is the bulk absorption loss, and FCP and FCN are the coefficients of the free-carrier loss.

Three different gain models can be used for the gain-guided laser calculation. The first model takes into account frequency dependence and can be used for spectral analysis. The second model is a simple empirical model and is valid for the lasing frequency. The third model is for the MQW model, which uses for the energy of bound states in the quantum well through solutions of a coupled set of Poisson and Schrödinger equations. The technique for simulating semiconductor lasers is to calculate forward bias

characteristics with gradually increasing voltage. Since the lasing spectrum is not the main subject matter in this dissertation work, the second and third gain models are chosen for the gain calculation. An example of an InGaAsP/InP double heterostructure (DH) laser has been simulated using the Silvaco Laser module. The gain curve verse input current is shown in Fig. 11.

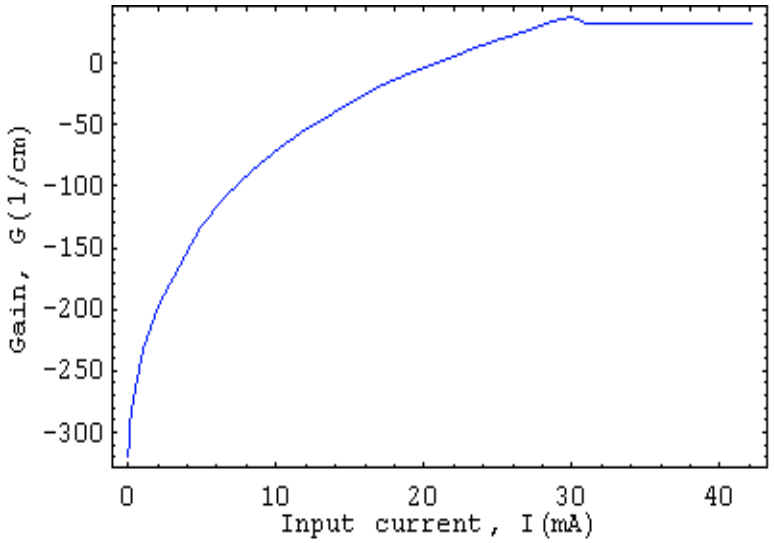

Figure 11. Gain curve for a DH InGaAsP/InP laser.

2.4.2 Simulation of Coupling Efficiency

There are several methods that can be used to analyze the coupling efficiency from semiconductor lasers to waveguides, including beam propagation methods (BPMs), finite difference time domain methods (FDTDMs), FEMs, and mode matching methods (MMMs). Conventional BPM is less suitable, given the high refractive index contrast between the semiconductor laser materials and the polymer waveguide materials. Finite element methods are the chosen, better alternative to analyze the problem. In this research work, the CAD tool, FEMLAB, is used to analyze the coupling efficiency from

the EEL to the polymer waveguide. FEMLAB is a powerful, interactive environment for modeling and solving scientific and engineering problems based on partial differential equations (PDEs). When solving the wave equation that describes an optical waveguide, FEMLAB applies a variation method based on FEM [62, 63]. FEMLAB runs FEM in conjunction with adaptive meshing, error control, and a variety of numerical solvers.

The calculation procedure for the application of the variation method to FEM is summarized as follows. The analysis region is first divided into segments which are called elements, and the function I_e is calculated for each element e. Then, the total functional I for the entire analysis region is obtained by summing up the function I_e for all elements: $I = \Sigma I_e$. The final eigenvalue equation is obtained by imposing the stationary condition on the function I [64].

Since the total function is a linear combination of the functions of the elements, the variation δI of the whole system is a sum of variation δI_e of each element e. Thus, $\delta I = \Sigma \delta I_e = 0$. The function I_e of an element e surrounded by the boundary Γ_e is given by [64]

$$I_e = \frac{1}{2}\left[\int\int_e \left\{\left(\frac{\partial \phi_e}{\partial x}\right)^2 + \left(\frac{\partial \phi_e}{\partial y}\right)^2 - k_0^2 (\epsilon_r - n_{eff}^2) \phi_e^2\right\} dxdy\right] - \left[\int_{\Gamma_e} \phi_e \frac{\partial \phi_e}{\partial n} d\Gamma\right] \quad (16)$$

where k_0 is the wave vector in free space, n is the normal vector, ϕ_e is the wave function, n_{eff} is the effective index, and ϵ_r is the relative permittivity. Next, the wave function ϕ_e can be expanded as [64]

$$\phi_e = \sum_{i=1}^{M_e} N_i \ \phi_{ei} = [N_e]^T \{\phi_e\} \tag{17}$$

where M_e is the number of nodes in element e and T is the transposing operator for a matrix. Then the basis function $[N_e]$ and the expansion coefficient $\{\Phi_e\}$ are expressed as $[N_e]= [N_1, N_2, N_3, \cdots, N_{Me}]^T$ and $\{\Phi_e\}= \{\Phi_1, \Phi_2, \Phi_3, \cdots, \Phi_{Me}\}^T$, respectively.

The function I_e given by Eq. 16 can thus be rewritten as [64]

$$I_e = \frac{1}{2} \{\phi_e\}^T ([A_e] - \lambda^2 [B_e]) \{\phi_e\} - \left[\int_{\Gamma_e} \phi_e \frac{\partial \phi_e}{\partial n} d\Gamma\right] \tag{18}$$

where matrixes $[A_e]$ and $[B_e]$ and the quantity λ^2 are given by [64]

$$[A_e] = \int\int_e \left(\frac{\partial [N_e]}{\partial x} \frac{\partial [N_e]^T}{\partial x} + \frac{\partial [N_e]}{\partial y} \frac{\partial [N_e]^T}{\partial y} \right) dxdy \tag{19}$$

$$[B_e] = \int\int_e [N_e][N_e]^T dxdy \tag{20}$$

$$\lambda^2 = k_0^2 (\epsilon_r - n_{eff}^2) \tag{21}$$

The function I_e can be obtained by summing up all the elements for the whole analysis region. Then, the line integral term in Eq. 18 is cancelled out since the wave function ϕ_e and its derivative with respect to the normal to the surface of the element e, $\partial\phi_e/\partial n$, are continuous at the boundaries with neighboring elements. After imposing the Dirichlet condition $\phi = 0$, where $\phi = \Sigma\phi_e$ at the boundaries, the function $I = \Sigma I_e$ for the whole analysis region can be obtained as [62-64]

$$I = \frac{1}{2} \{\phi\}^T ([A] - \lambda^2 [B]) \{\phi\} \quad (22)$$

where $[A] = \Sigma A_e$ and $[B] = \Sigma B_e$ [62-64]. Basically, solving the wave equation is equivalent to solving the eigenvalue matrix Eq. 23 [62-64].

$$([A] - \lambda^2 [B]) \{\phi\} = 0 \quad (23)$$

Figure 12(a) shows a simulation example of the optical wave incident normally on the surface of a dielectric medium using FEMLAB. The transverse electric (TE) wave transmits from the air to the dielectric medium with an index of refraction 1.5. Figure 12(b) shows that the transmission coefficient, T, as a function of number of mesh elements per unit area, N, is calculated using FEMLAB. The transmission coefficient is calculated to be 96% using Fresnel formula. After $N = 1\times10^{15}$, the numerical error is estimated to be 2.69%. The mesh size, $N \geq 1\times10^{15}$, per unit area will be used in Section 4 to construct a theoretical model of the laser coupling efficiency to the waveguide as a function of laser to waveguide separation.

2.1 Summary and Discussion

The approach to InGaAsP/InP EEL and BCB waveguide analysis has been presented in this chapter. There are several factors which affect threshold current in EELs, such as cavity length, facet reflectivity, optical confinement factors, active layer thickness, device temperature, and transparent carrier density. The commercial software, Silvaco, is used to analyze these parameters in the thin film EEL devices developed in this dissertation. In this Silvaco Laser program, Helmholtz equation, Poisson equation, Schrödinger

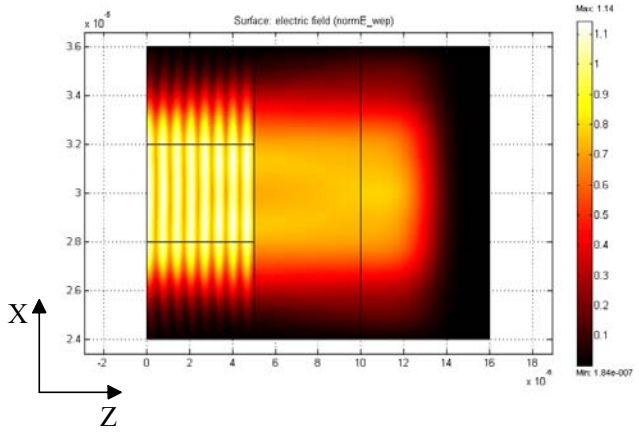

(a)

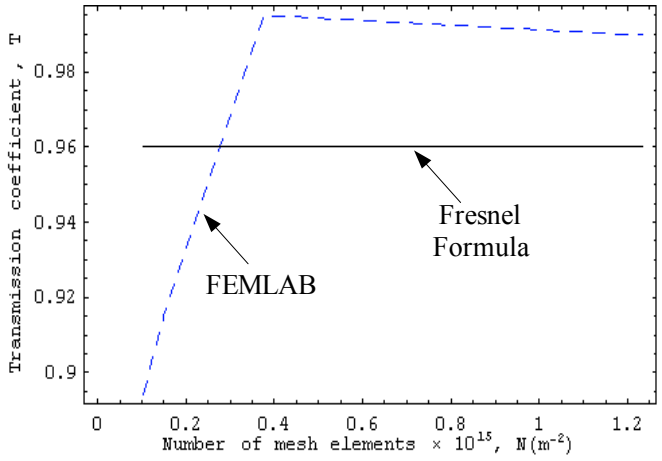

(b)

Figure 12. (a) Electric field distribution on XZ plane; (b) Transmission coefficient, T, as a function of number of mesh elements per unit area, N.

equation, and diffusion equations are solved self consistently. In this dissertation, the core of the planar optical waveguide is composed of a BCB polymer due to the relatively low loss at a wavelength of 1.3 μm. For guided mode operation, the BCB film is deposited on substrate with refractive index lower than 1.52. The end facet coupling method is employed to excite guided waves in the BCB waveguide. The analysis of the coupling efficiency from thin film EELs to BCB waveguides will be discussed in Chapter 4 using FEMLAB based on FEM.

CHAPTER 3

DEVICES DESIGN, FABRICATION, INTEGRATION, AND CHARACTERIZATION

3.1 Introduction

The monolithic integration of polymer waveguides and thin film optoelectronic devices has been discussed for applications such as optical interconnections [65-69]. In this dissertation research, thin film EELs emitting at a wavelength of 1.3 μm are used as an optical source for integration with polymer waveguides. EELs have been a topic of research interest for many years, and long lifetime, stable, high-powered, and inexpensive EELs are being used for many products, including compact disk (CD) players, digital video disk (DVD) players, and laser pointers. Since the output profiles of EELs are essentially elliptical in shape, the profiles are well suited for launching directly into a channel waveguide. The use of polymer waveguides and the potential integration of these optical interconnections onto low cost epoxy and polymer substrates are particularly interesting toward pervasive and low cost implementations. Thus, the use of polymer waveguides for low cost optical interconnections that are process compatible with current board, module, and integrated circuit technology is a research goal. In this chapter, thin film InGaAsP EELs and polymer channel waveguides are designed, fabricated, integrated, and tested. The optical output beam of the EELs is launched into the waveguides, and the laser optical output from the waveguide core is measured.

3.2 Design of Thin film InGaAsP/InP EELs and BCB Waveguides

In order to fabricate thin film InGaAsP/InP multiple quantum well (MQW) EELs, the first step is to define a structure suitable to be processed into thin film lasers. InGaAsP/InP (MQW) lasers emitting at 1.3 μm are designed for this research. The epitaxial layer structure is shown in Table 4. The function for each layer in the structure is described as follows.

The ohmic contacts are formed on the 19th layer with p^+ doping and the 5th layer with n^+ doping. The thickness of these layers are 0.1 μm and 0.2 μm, respectively. The 18th

Table 4. InGaAsP/InP laser layer structure.

Layer	Material	Thcikness (nm)	Doping (cm^{-3})	Dopant
19	InGaAs	100	1×10^{18}	Zinc
18	InP	1000	1×10^{18}	Zinc
17	InGaAsP	150	1×10^{17}	Zinc
16	InGaAsP	6		None
15	InGaAsP	10		None
14	InGaAsP	6		None
13	InGaAsP	10		None
12	InGaAsP	6		None
11	InGaAsP	10		None
10	InGaAsP	6		None
9	InGaAsP	10		None
8	InGaAsP	6		None
7	InGaAsP	150		None
6	InP	1000	1×10^{17}	Sulphur
5	InGaAs	200	5×10^{17}	Sulphur
4	InP	2000		None
3	InGaAs	200		None
2	InP buffer	500		None
1	InP			None

and the 6th layers are both outer cladding layers (1 μm thick) and are doped by Zn and S, respectively. The saturation level of zinc in InP occurs at around 1.5-2×10^{18} cm^{-3} [70, 71].

Above 1×10^{18} cm^{-3}, diffusion of the zinc into the underlying undoped InGaAsP layers becomes a problem because it is detrimental to the laser diode performance [72]. Thus, the zinc doping is at a level of 5×10^{17} cm^{-3} for ~0.3 μm of the p-InP (close to the 1 μm layer). The doping level is then increased to 1×10^{18} cm^{-3} for the remainder of this layer. This has the effect of reducing the zinc diffusion into the active layer.

Both the 7th and the 17th are undoped inner cladding layers with 0.15 μm thick. In order to confine the optical modes in the active region, the thickness of the inner cladding layers are designed to be much thicker than that of the active layers. Figure 13 is the near field mode pattern of the fundamental mode in the designed structure as modeled using Laser module in Silvaco.

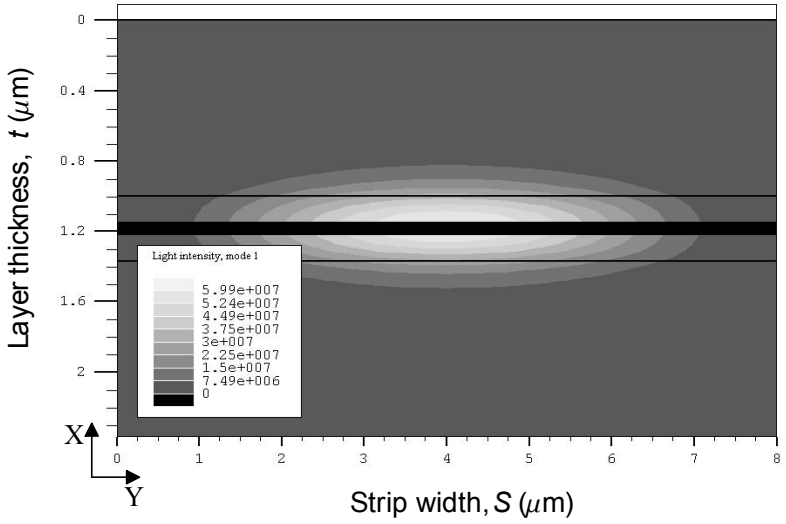

Figure 13. Near field pattern of the fundamental mode in the designed thin film EELs.

Layers 8th to 16th in the design are the unstrained MQW regions, which provide gain, and lase at a wavelength of 1.3 μm. The thickness of the $In_xGa_{1-x}As_yP_{1-y}$ well, where x = 0.66 and y = 0.73, is 6 nm. The thickness of the $In_xGa_{1-x}As_yP_{1-y}$ barrier, where x = 0.85 and y = 0.33, is 10 nm. The gain of the active region, G, in the designed structure as a function of input current density, J, is shown in Fig. 14. In this analysis, the length of the laser material is 400 μm and the mirror reflectivity is 28% (calculated using Fresnel formula). This is modeled using Silvaco Laser module. In Fig. 14, the material gain is saturated at 261.6459 A/cm^2, which indicates that the quasi-Fermi levels are pinned at the threshold position.

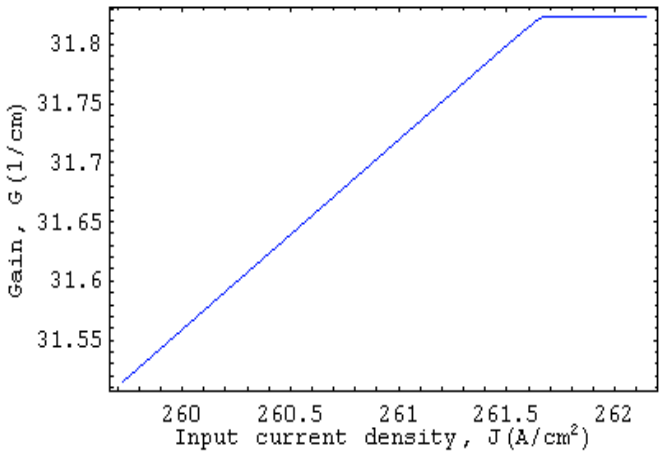

Figure 14. Gain as a function of injected current density.

The 3rd layer, InGaAs, is the stop etching layer to prevent the further etching into the laser structure during the removal of the InP growth substrate. The thickness for the layer is 0.2 μm. The 4th layer, InP, is another stop etching layer and is also a supporting layer to reduce the curvature of the thin film epilayers after the removal of the InP growth substrate. The thickness of this layer is 2 μm.

The polymer channel waveguides are designed for guided-mode operation in this dissertation. The planar structure is shown in Table 5. The purpose of the BCB layer is to act as the waveguide core layer. The refractive index of the BCB layer at wavelength of 1.31 μm is 1.52 [35]. The purpose of the SiO_2 layer is to act as the waveguide cladding layer. The refractive index of the SiO_2 is 1.45 which is measured using Ellipsometer. This is an asymmetric channel waveguide. The width of the polymer waveguide is 100 μm in order to maximize coupling of the emitted output from the laser. The near field pattern of the fundamental mode in the polymer channel waveguide was modeled using FEMLAB and is shown in Fig. 15.

Table 5. CYCLOTENE BCB 3022-46 channel waveguide layer structure.

Layer Number	Material	Thcikness (μm)	Refractive Index
3	BCB	5	1.52
2	SiO_2	10	1.45
1	Si (substrate)	500	

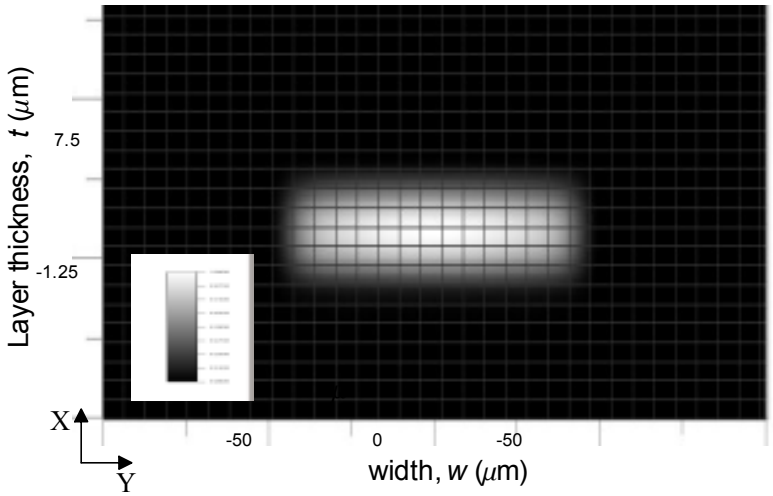

Figure 15. Near field pattern of the fundamental mode in polymer channel waveguide.

3.3 Fabrication of Thin Film InGaAsP/InP EELs and BCB Waveguides

The processing steps used to fabricate thin film lasers are shown in Fig. 16. InP/InGaAsP wafers are first cleaved into 0.5 cm × 0.5 cm samples. Samples are then coated with Si_3N_4 (3000 Å) in a plasma enhanced chemical vapor deposition (PECVD) system ($SiH_4/N_2/NH_3$: 100 sccm/300 sccm/3 sccm) for 30 minutes. The 300 μm wide and 5 μm deep mesa patterns are defined on samples using an inductively coupled plasma (ICP) dry etch system (CF_4 = 30 sccm) and a reactive ion etching (RIE) system (CH_4/H_2: 12 sccm/40 sccm) and stopped etching on InGaAs layer (layer 3 in Table 4).

The 20 μm wide laser stripes are defined on top of the Si_3N_4 layer in the ICP, p-contact metals Ti/Pt/Au (300/400/3000 Å) are deposited using an electron beam evaporator (e-beam) system, followed by annealing of the p-contact metals at 380 ºC for 1 min to form ohmic contacts. The p-contact sides of the laser samples are then coated with Apizeon wax and are attached to a glass slide. The laser samples are then soaked in HCl/H_2O (2:1) for 5 hours to completely remove the InP substrate. The broad area n-type Ni/AuGe/Ti/Au (300/400/200/4000 Å) contact is deposited on the released side of the lasers samples in the filament evaporator. The thin epilayers are then transferred to a flexible metal carrier from the glass slide. By bending the flexible carrier, the laser samples are cleaved in the wedge direction. After soaking in TCE, each thin film laser die is detached from the flexible carrier and transferred onto a transfer diaphragm. Each thin film laser die on the diaphragm is transferred to p-contact pads on SiO_2/Si host substrates to be characterized or integrated with polymer waveguides.

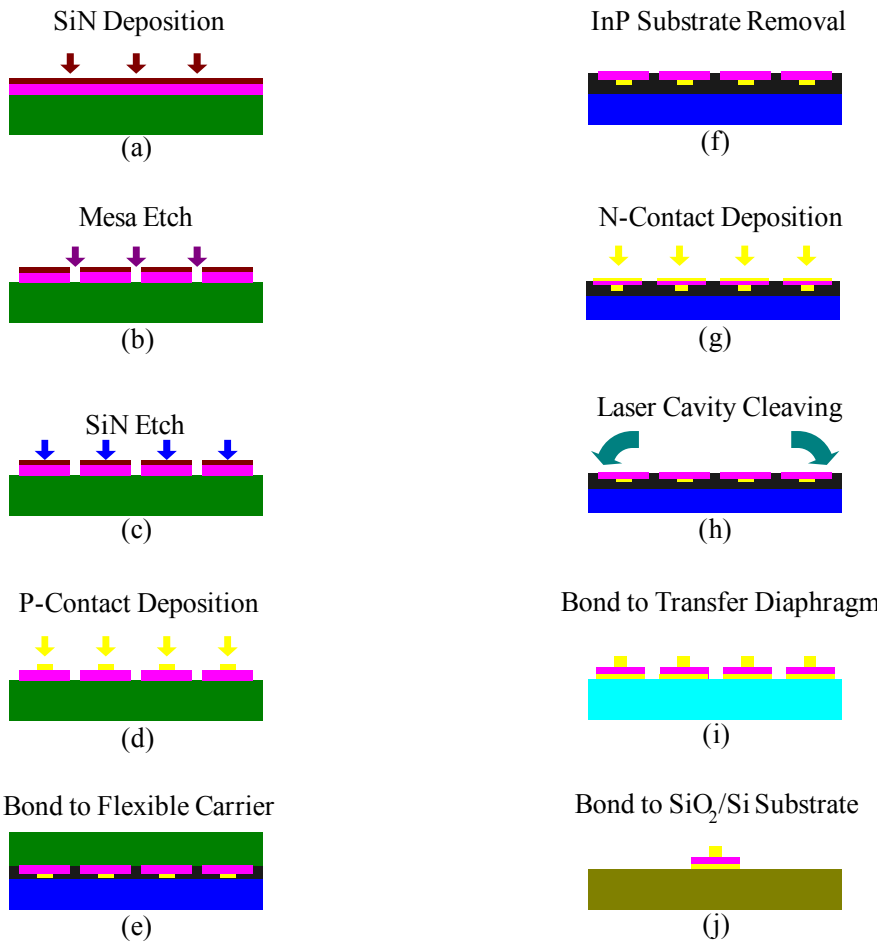

Figure 16. Fabrication process of thin film EELs.

Thin film unstrained InP/InGaAsP MQW lasers have been fabricated for this dissertation, as shown in Fig. 17(a). In Fig. 17(a), the cleaved InP/InGaAsP MQW thin film lasers are attached to a flexible carrier with Apizeon wax. The cleave (visible vertical lines between the lasers) is propagated from the wedge direction. The lasers are detached and bonded onto an Au/SiO_2/Si host substrate, as shown in Fig. 17(b). The strip width on top of the device is 20 μm. The device thickness is 5 μm, the cavity length is 400 μm, the width is 300 μm, and the wedge is 100 μm. The cleaved facet of a 5 μm thick thin film laser on an Au/SiO_2/Si substrate is photographed, as shown in Fig. 17(c). These are the first reported thin film InP-based laser less than 10 μm thick.

Due to the requirement of deep etching of the InGaAsP/InP material in RIE, a series of experiments were carried out for a high rate CH_4: H_2 plasma etching process without undesirable re-deposition from the dry etch system. The etch depth was measured with an Alpha step profiler. The etch mask consisted of a 2000 Å Al layer. To guarantee consistency between each run, the chamber was cleaned using an O_2 plasma to remove deposited materials from the dry etch chamber before loading the samples. The measured etch rate with respect to pressure, gas flow rate, and CH_4 concentration is given in Table 6.

As seen in Table 6, the etch rate increases linearly with methane gas flow rate; however, heavy re-deposited material formation on the sample surface roughened the surface and contaminated the chamber. In addition, the polymer redeposition prevented further processing of the thin film EELs after removing the growth InP substrate because the sample adhered strongly to the carrier. In this research, the CH_4 : H_2 mixture rate in

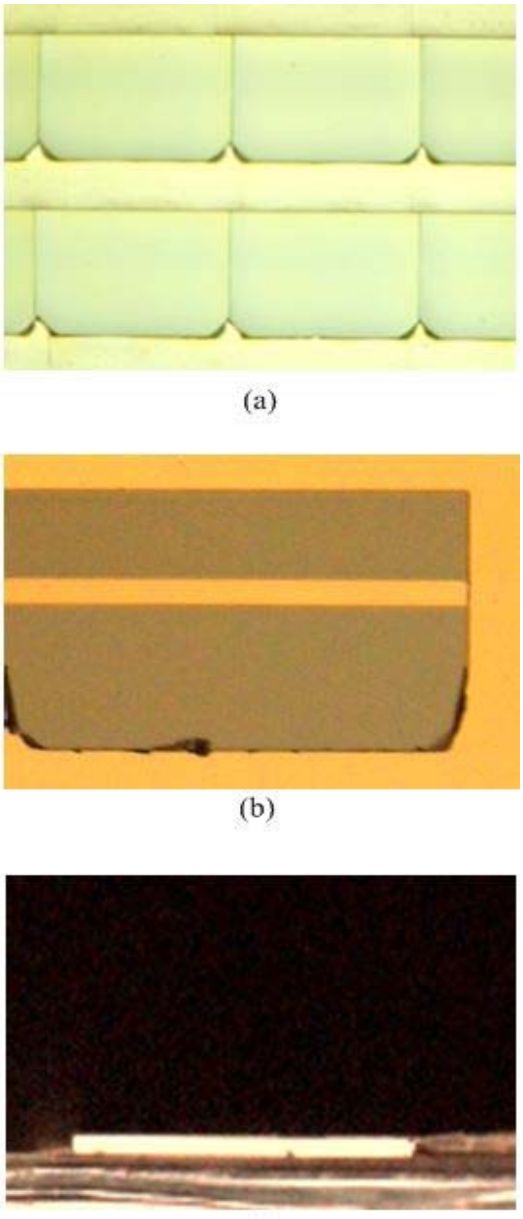

Figure 17. (a) Thin film lasers on a flexible carrier; (b) A thin film EEL on the edge of an $Au/SiO_2/Si$ substrate; (c) Cleaved facet of a thin film laser.

the 10th experiment was adapted to perform the deep mesa etch (3 μm). With the addition of oxygen to the CH_4 : H_2 mixture, a better etch rate, 40 nm/mins, was achieved.

Table 6. Experimental results of reactive ion etching of InP.

	RF power (w)	Pressure (mtorr)	DC (V)	Ref	CH4 (sccm)	H2 (sccm)	Etch rate (nm/min)
1	400	17	250	5	7	52	4.26
2	400	17	250	5.3	14	52	10
3	400	32	250	6.7	7	52	12.13
4	400	32	250	4.8	14	52	12.36
5	400	72	250	4.8	7	52	15.04
6	400	50	250	2.7	14	52	20.23
7	400	50	250	2.7	17	42	67.76
8	400	50	250	3.7	30	42	80.96
9	400	50	250	3.7	30	15	90.96
10	400	50	250	4.8	12	40	34

3.4 Integration of Thin Film InGaAsP/InP EELs with BCB Waveguides

The steps toward integration of a thin film edge emitting laser and a polymer channel waveguide are shown schematically in Fig. 18. For integration with a polymer channel waveguide, a thin film laser die on a diaphragm is transferred to p-contact pads on a 3 cm × 3 cm Si substrate. The substrate is coated with SiO_2 at a thickness of 5 μm in the PECVD system (SiH_4/N_2O: 100 sccm/250 sccm for 2 hours). The length and width of the contact pads are designed as 500 μm and 400 μm, respectively. The size of the pads is larger than the EEL size for heat dissipation using an anneal from the EEL substrate. The thin film lasers are bonded to the pads on the SiO_2/Si substrate at a temperature of 150ºC for one hour.

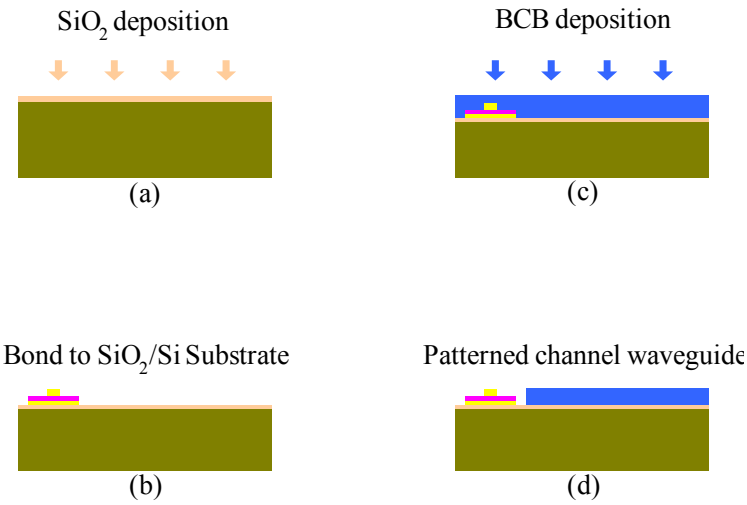

Figure 18. Integration of a thin film EEL and a channel waveguide.

In order to fabricate the BCB waveguide, liquid adhesion promoter is dispensed onto the laser/SiO_2/Si substrate surface at 500 rpm for 20 seconds. The substrate is then spun at 3000 rpm for 30 seconds to dry and is then coated with a 5 μm thick BCB layer which is cured to ensure resistance to subsequent processing steps. A hard cure profile to reach full cure (95% degree of polymer conversion) using a convection oven is given in Table 7 [73]. The final step is to cut the waveguide channel. A channel waveguide is patterned using a 1000 Å thick Ti mask and then the BCB is etched using an ICP system (CF_4/O_2 : 40 sccm/30 sccm). The BCB polymer on both sides of the laser cavity is removed completely to provide enough facet reflectivity for the thin film laser to lase. To analyze the coupling efficiency from the laser to the waveguide, the separation of the front facet of the laser to the entrance facet of the channel waveguide was varied in this research, and is compared to theoretical calculation in Chapter 4.

Table 7. Hard cure temperature profile.

	Ramp schedule	Soak time
Step 1	5 mins. ramp to 50 ºC	5 min.
Step 2	15 mins. ramp to 100 ºC	15 min.
Step 3	15 mins. ramp to 150 ºC	15 min.
Step 4	60 mins. ramp to 250 ºC	60 min.
Step 5	Natural cool down	

Thin film EELs have been integrated with polymer waveguides and have also been embedded into polymer waveguides as part of this dissertation research, as shown in Fig. 19(a) and Fig. 19(b). Figure 19 shows photomicrographs of two implementations of thin film edge emitters integrated with BCB polymer waveguides. In the first implementation, the thin film emitter front facet is fully embedded in the polymer waveguide. In the second implementation, the polymer waveguide is fabricated on a SiO_2/Si substrate with a 3 μm separation between the end of the waveguide and the thin film EEL. In both cases, the width and the thickness of the polymer waveguides are 100 μm and 5 μm, respectively. The contact strip is 20 μm for both cases, as well.

3.5 Characterization of Thin film InGaAsP/InP EELs and BCB Waveguides

In order to characterize the output power of the thin film lasers, the devices were transferred from the transfer diaphragm to p-contact pads on SiO_2/Si substrates and tested by applying a pump current from a current source (100 μs pulse duration and 5% duty cycle operation, ILX Lightwave LDP-3811). The measurement setup for the thin film laser and channel waveguide on the SiO_2/Si substrates is shown in Fig. 20.

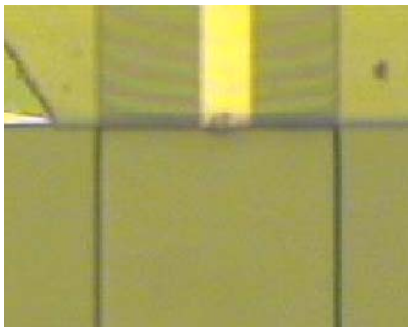

(a)

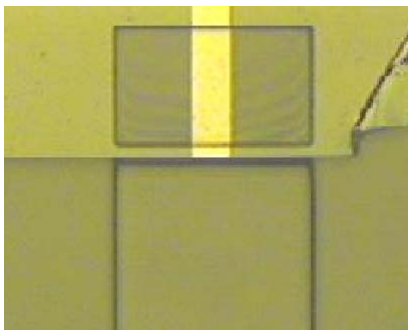

(b)

Figure 19. (a) An embedded thin film emitter in the waveguide; (b) A thin film EEL integrated with the waveguide with a 3 μm gap.

Two types of integration structures were characterized: the thin film lasers bonded to the edge of SiO_2/Si substrate and the thin film lasers integrated next to the polymer waveguide. For the first case, the output power from the thin film laser was measured. For the second cases, the laser/SiO_2/Si substrates were cleaved along the transverse direction of the polymer waveguide. The pumping current was applied to the thin film laser by the current source. With the use of an infrared imaging system, images of the light coupling from the laser to the waveguide as well as the near field pattern of the waveguide output facet can be photographed. The output power from the waveguide end facet was measured by coupling the light into a photodetector (with responsivity of 0.89

mA/mW at a wavelength of 1.31 μm). The detector's photocurrent was measured using a source measurement unit (SMU Keithley 236). By recording the light output power with respect to the input current, the output power verse input current curve was generated, commonly referred to as an LI curve. The slope efficiency, ΔP/ΔI (mW/mA), of the L-I curve is referred to as the external quantum efficiency, η_d, by multiplying 2qλ/hc [39], where q is 1.6022×10^{-19} C, λ is 1.31×10^{-6} m, h is 6.6262×10^{-34} J·sec, and c is 3.0×10^{8} m/sec.

The lasers with 400 μm cavity length were characterized using a 100 μs pulse duration and 5% duty cycle operation. The threshold current of the thin film lasers was measured as 30 mA, as shown in Fig. 21(a). An infrared image of the near field output of

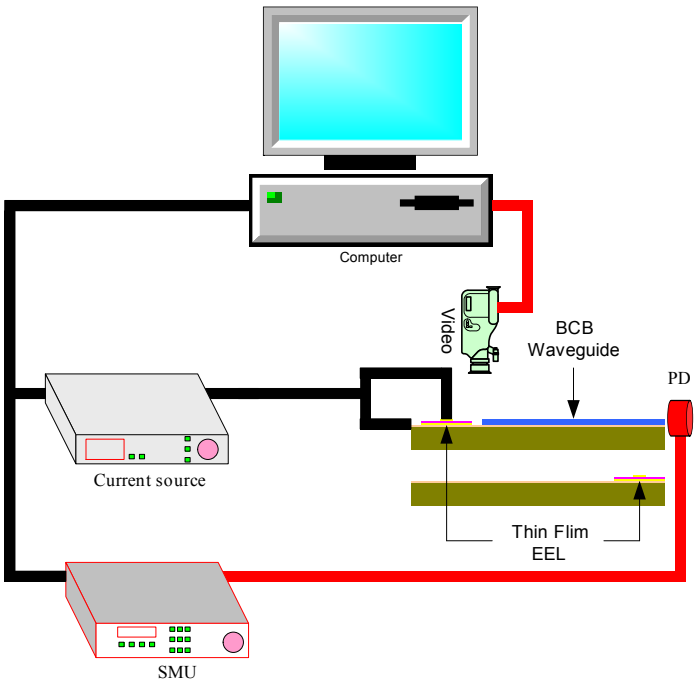

Figure 20. Testing setup of thin film EELs and waveguides on SiO_2/Si substrates.

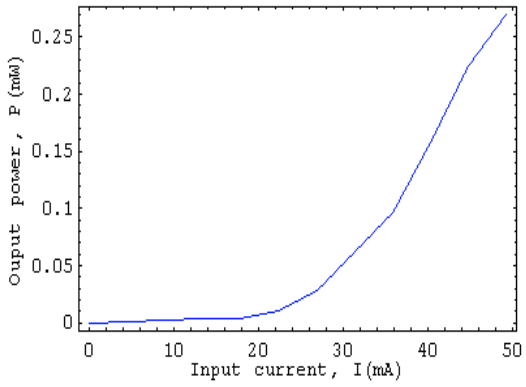

(a)

(b)

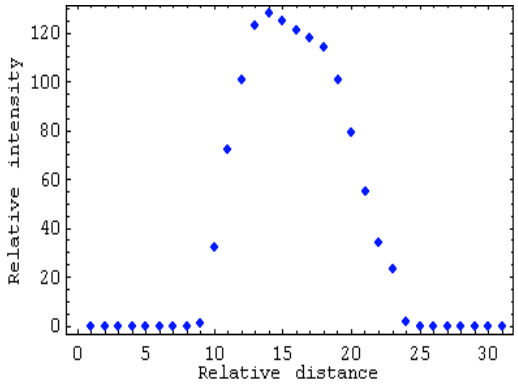

(c)

Figure 21. (a) L-I curve of thin film EELs; (b) The near field pattern on the thin film EEL facet; (c) The intensity distribution along the vertical direction.

the laser at a drive current of 49 mA was photographed, as shown in Fig. 21(b). The relative intensity of the near field pattern was measured along the direction parallel to the growth direction at the center of the contact stripe, which approximates a Gaussian shape, as shown in Fig. 21(c). The beam width at the laser facet is estimated at 2 μm. The slope efficiency for the thin film EEL is estimated at 2%. This is the first demonstration of InP-based thin film EELs less than 10 μm, which are suitable for heterogeneous integration.

The output light from the laser is coupled into the waveguide by end facet coupling. With the use of an infrared imaging system, images of the light coupling from the laser to

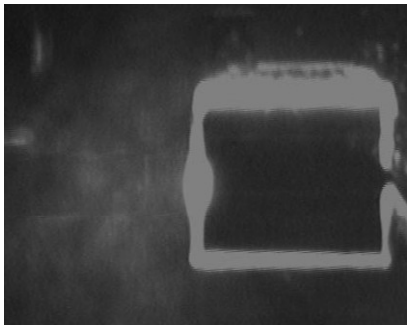

(a)

(b)

Figure 22. (a) Infrared image of thin film EEL coupling to BCB waveguide; (b) The near field pattern on the waveguide facet.

the waveguide can be imaged, as shown in Fig. 22(a). An infrared image from the end of the waveguide facet was also taken, as shown in Fig. 22(b). Since the channel waveguide is softened at the corners after curing, the pattern in Fig. 22(b) is not rectangular around the edge. Thin film lasers integrated next to polymer waveguides with gap distance 3 μm were characterized with 5% duty cycle and 100 μs pulse width. The measured output power from the waveguide end facet at a drive current of 49 mA for the BCB waveguide of length 2.8 mm was 0.038 mW. In addition, the L-I curves of integration structures with the gap distance of 5 μm, 8 μm, and 10 μm were characterized under the same testing conditions to compare the optical output power as a function of laser to waveguide separation, as shown in Fig. 23. The waveguide length for the gap distance of 5 μm, 8 μm, and 10 μm is 3.9 mm, 2.4 mm, and 3.7 mm, respectively. The power coupling decreases with increasing the gap distance, which indicates that the less optical power is transferred into the optical waveguide with the large separation between the thin film EEL and the waveguide.

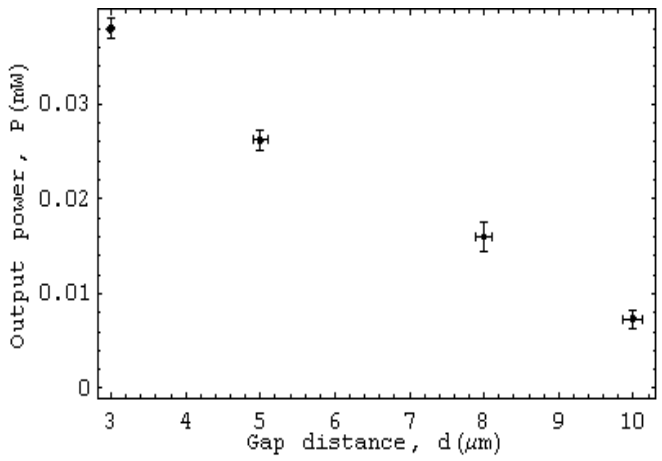

Figure 23. Measured output power from the waveguide end facet at drive current 49 mA.

3.6 Summary and Discussion

The fabrication and integration of a thin film EEL whose optical output is coupled into a polymer waveguide integrated on the same electrical interconnection substrate is reported in this dissertation. It is the first demonstration of thin film MQW InGaAsP/InP EELs with a thickness less than 10 μm. The heterogeneous integration of this MQW InGaAsP/InP EEL with a polymer waveguide structure is a fundamental building block toward the realization of planar lightwave circuits in an embedded optical interconnection format. The demonstration of a thin film laser embedded in a waveguide eliminates the need for either an external optical source coupled to the waveguide or a bump bonded optical source with a beam turning element to launch an optical wave into the waveguide. The laser threshold current is 30 mA, and the output is approximated as a Gaussian spatial shape. The output of the waveguide is also measured, which indicates that the laser lases, is coupled to the polymer waveguide, and that the waveguide propagates the optical beam successfully. Thus, the potential of an embedded optical waveguide output on an electrical interconnection substrate has been realized.

CHAPTER 4

LASER TO WAVEGUIDE COUPLING EFFICIENCY THEORY AND COMPARISON OF THEORY TO EXPERIMENT

4.1 Introduction

For the design of thin film EELs integrated with polymer waveguides (CYCLOTENE 3022-46 BCB), a fundamental knowledge of coupling efficiency from the lasers to the waveguides is crucial. There are several factors contributing to the coupling efficiency in the integration structure, such as the similarity of mode profiles in the laser cavities with those in the polymer waveguides, the entrance facet profiles of the polymer waveguide, the launch position of the optical field from the lasers, and the alignment between the lasers and the waveguides. In this chapter, optical modes in the laser cavities and in the polymer waveguides are analyzed using the thin film transfer matrix method. Next, the coupling efficiency is calculated using the optical modes in the laser cavities. The FEM is adapted to perform the analysis of coupling efficiency due to the strong refractive index contrast between the laser cavities (n_r ~3.2) and the polymer waveguides (n_r ~1.5). The coupling efficiency as a function of gap distance is presented. The effect of waveguide facet profile on coupling efficiency is also investigated. For the design of fully embedded thin film lasers in waveguides, the threshold current and output power are predicted theoretically. Finally, the calculated optical output power from the end facet of the polymer waveguide is compared to the experimentally based estimates.

4.2 Optical Modes in InGaAsP/InP MQW Lasers and Polymer Waveguides

The schematic diagram of a thin film EEL integrated with a polymer waveguide is shown in Fig. 24. In Fig. 24, an air gap discontinuity from z = 0 to z = d is located between a MQW semiconductor waveguide and a polymer waveguide. The length of the laser cavity, L_1, is 400 μm. The length of the polymer waveguide, L_2, is 10 μm. The thickness of the thin film EEL, the polymer waveguide, and the SiO_2 are h_1 = 5 μm, h_2 = 5 μm, and h_3 = 5 μm, respectively. The optical wave travels from the semiconductor waveguide to the air and then to the polymer waveguide and crosses a discontinuity plane at z = 0 and at z = d. The refractive index for SiO_2 is 1.45. The refractive index for InP, InGaAsP (λ = 1.3 μm), and InGaAsP (λ = 1.1 μm) are 3.22, 3.52, and 3.33, respectively [74]. The refractive index for the polymer waveguide is 1.52. Both the semiconductor waveguide and the polymer waveguide are assumed to be lossless to simplify the calculation complexity. The transverse electric (TE) modes are considered only in this research since the lasing of TE modes in unstrained semiconductor lasers occurs preferentially [75].

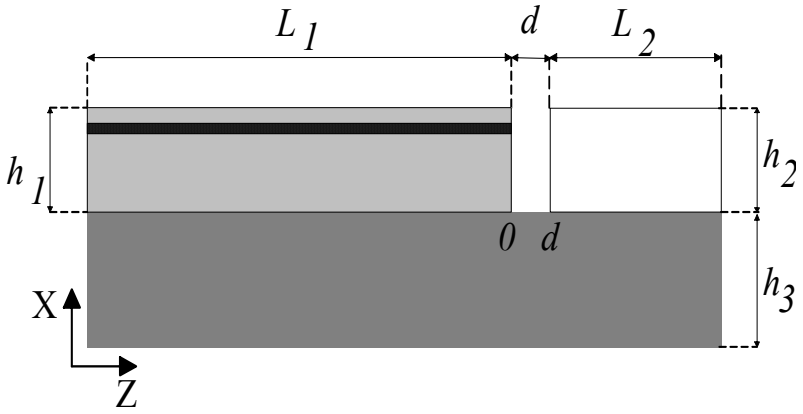

Figure 24. Schematic diagram of the integration structure.

There is no polarization cross coupling when the wave is transmitted from the semiconductor waveguide to the air and then to the polymer waveguide. The analysis starts by solving the existing transverse mode functions in a MQW slab waveguide to insert them into the commercial FEM software, FEMLAB, to complete the coupling efficiency calculation.

A MQW semiconductor waveguide can be simplified as a multilayer dielectric lossless waveguide and can be solved using the thin film transfer matrix formulation [76]. A multilayer nonmagnetic slab waveguide structure is shown in Fig. 25. In Fig. 25, X_i represents each discontinuity point. The cover region is above X_n and the substrate region is below 0. The thickness for both the cover region and the substrate region are extended infinitely. The permittivity for each waveguide layer is characterized by $\varepsilon_0\varepsilon_i$ where ε_0 is the permittivity in vacuum and ε_i is the relative permittivity for each specific layer in Fig. 25.

An optical wave travels along the $+z$ direction out of the paper. For the TE mode case, the electric field propagating in the i-th layer is $E_{yi}(x, z) = \mathcal{E}_{yi}(x)e^{j(\omega t-\beta z)}$. The

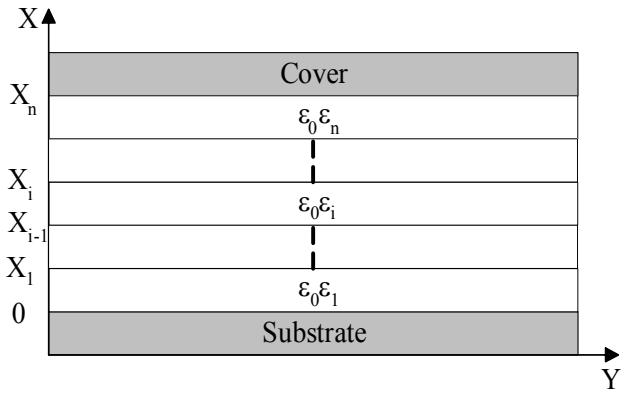

Figure 25. Geometry of a multilayer lossless waveguide structure.

magnetic (H) field is derived using Maxwell's equations $\nabla \times E_i = -j\omega\mu_0 H_i$ and $\nabla \times H_i = j\omega\varepsilon_0\varepsilon_i E_i$. The field components, $\boldsymbol{\mathcal{E}}_{yi}(x)$ and H_{zi}, tangential to the boundary in the i-th layer are related to each other by Eq. 22 in the matrix form [76].

$$\begin{pmatrix} \frac{d}{dx}\,\boldsymbol{\mathcal{E}}_{yi}(x) \\ \frac{d}{dx}\,\omega\mu_0 H_{zi}(x) \end{pmatrix} = \begin{pmatrix} 0 & -j \\ -jk_{xi}^2 & 0 \end{pmatrix} \begin{pmatrix} \boldsymbol{\mathcal{E}}_{yi}(x) \\ \omega\mu_0 H_{zi}(x) \end{pmatrix} \tag{24}$$

where $k_{xi}^2 = n_i^2 k_0^2 - \beta^2$, $n_i^2 = \varepsilon_i^2$, $k_0 = 2\pi/\lambda$, and λ is the free space wavelength. The electrical tangential components u_i are continuous at x_i, $u_i(x_i) = u_{i-1}(x_i)$ and the magnetic tangential components v_i are also continuous at x_i $v_i(x_i) = v_{i-1}(x_i)$, $i = 0,1,2\ldots n$. Using this boundary condition and Eq. 10, the fields tangential to the boundaries $u_s(0)$ and $v_s(0)$ at the top of the substrate layer are related to those tangential to the boundaries $u_b(x_n)$ and $v_b(x_n)$ at the bottom of the cover layer by Eq. 23 [76].

$$\begin{aligned} \begin{pmatrix} u_b(x_n) \\ v_b(x_n) \end{pmatrix} &= M_n M_{n-1} M_{n-2} \cdots M_1 \begin{pmatrix} u_s(0) \\ v_s(0) \end{pmatrix} \\ &= \begin{pmatrix} m11 & m12 \\ m21 & m22 \end{pmatrix} \begin{pmatrix} u_s(0) \\ v_s(0) \end{pmatrix} \end{aligned} \tag{25}$$

where M_i is denoted as

$$M_i = \begin{pmatrix} \mathrm{Cos}[k_{xi} h_i] & \frac{-j}{k_{xi}} \mathrm{Sin}[k_{xi} h_i] \\ -jk_{xi}\,\mathrm{Sin}[k_{xi} h_i] & \mathrm{Cos}[k_{xi} h_i] \end{pmatrix}. \tag{26}$$

Considing only the guiding modes, the electric field is zero at $x \to \infty$ and $x \to -\infty$. By using the boundary conditions, the characteristic equation is derived as Eq. 27 [76]. The zeros of Eq. 27 are the propagation constants, β.

$$\mathrm{Det}\begin{bmatrix} 1 & -(m11 + jk_s\, m12) \\ -jk_c & -(m21 + jk_s\, m22) \end{bmatrix} = 0 \tag{27}$$

The optical mode in the semiconductor waveguide was simulated using the thin film transfer matrix method, as shown in Fig. 26. The effective index of the TE_0 mode in the semiconductor waveguide was estimated to be 3.267. Figure 26 shows the power distribution in the semiconductor waveguide. The MQW layer region ranges from 0.15 μm to 0.22 μm. The two inner cladding InGaAsP layers range from 0 to 0.15 μm and from 0.22 μm to 0.37 μm, respectively. The two outer cladding InP layers range from -1μm to 0 and from 0.37 μm to 1.37 μm, respectively.

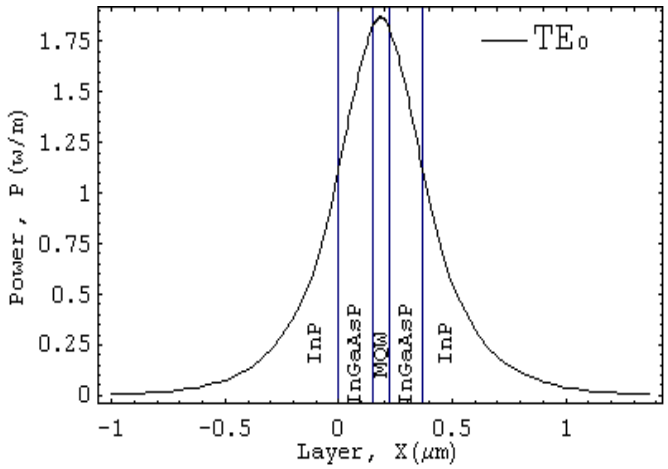

Figure 26. TE_0 mode pattern in the semiconductor waveguide.

The TE_0 mode, the TE_1 mode, and the TE_2 mode in the BCB waveguide were simulated using the thin film transfer matrix method, respectively, as shown in Fig. 27. The core layer ranges from 0 to 5 μm. The substrate layer and the cover region range from –1 μm to 0 and 5 μm to 6 μm, respectively. The effective indices of the TE_0 mode, TE_1 mode, and TE_2 mode in the polymer waveguide were calculated as 1.51556, 1.50229,

and 1.48044, respectively. Most of the optical power is carried in the fundamental mode. In Fig. 27, the power distribution in the optical modes is not symmetric since the refractive index difference between the waveguide core and the substrate cladding is smaller than that between the waveguide core and the cover region. Comparing Fig. 26 with Fig. 27, the result indicates that most of the optical power coupling occurs between the TE_0 in the laser cavity and in the polymer waveguide, due to the mode profile similarities.

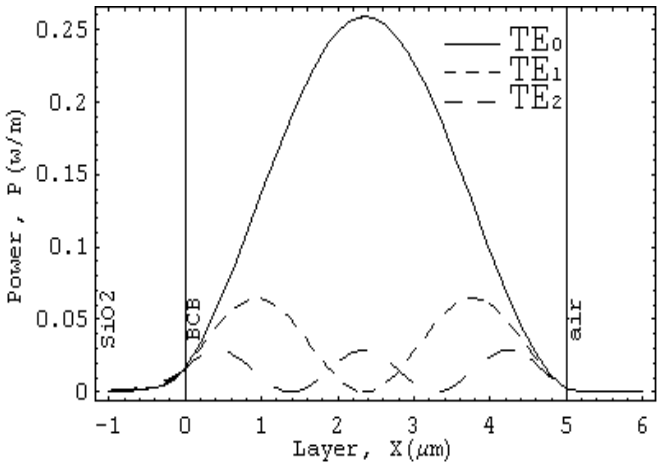

Figure 27. Optical modes in the BCB waveguide.

4.3 Coupling Efficiency from the Lasers to the Waveguides

The fields derived from the thin film transfer matrix formulation were used as the incident fields in the analysis of the coupling efficiency using FEMLAB. The coupling efficiency from the semiconductor waveguide to the polymer waveguide in Fig. 24 is defined as P_t/P_i, where P_t is the transmitted power measured at the point $Z = d+5$ μm in Fig. 24 from the incident waveguide facet at d, and P_i is the total incident power into the semiconductor waveguide. In this research, the P_t/P_i is analyzed for different gap distances between the semiconductor waveguide and polymer waveguide, from 0 μm to

10 µm. The theoretical optical output power from the end facet of the polymer waveguide are compared to those estimated from the experimental results for the gap distances 3 µm, 5 µm, 8 µm, and 10 µm.

A sample simulation result of the power distribution on the XZ plane is shown in Fig. 28. The material growth direction is along the X axis. The light beam transmits from Z = 0 µm to Z = 5 µm. The entrance facet of the polymer waveguide is at Z = 5 µm. The angle of the waveguide entrance facet is $\theta = 90^{o}$. The launch position of the electric field is at X = 2.8 µm and Z = 0. The air gap between the thin film laser and the polymer waveguide is 5 µm. The coupling efficiency is calculated as a function of gap distance, as show in Fig. 29(a). There are 100 calculated data points. For example, for the cases of gap distance 0 µm, 3 µm, 5 µm, 8 µm, and 10 µm, the coupling efficiencies are calculated to be at 0.9282, 0.3949, 0.3289, 0.2665, and 0.20, respectively. The coupling exponentially decreases as the gap increases distance from 0 to 3 µm. For gap distances

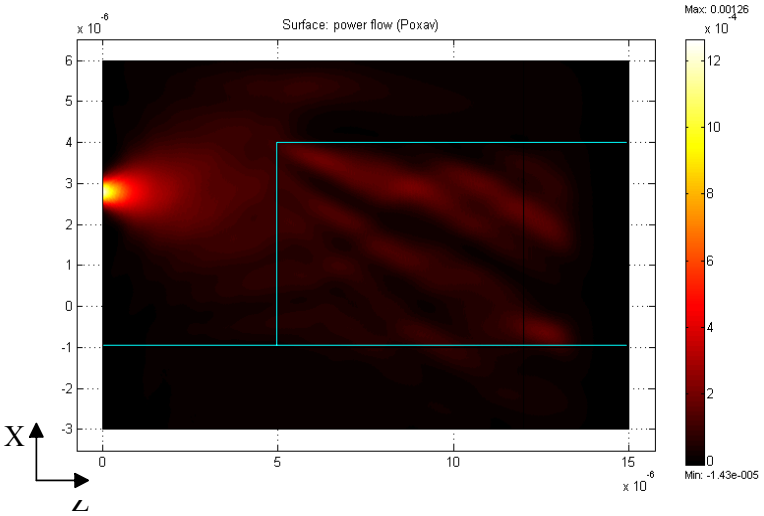

Figure 28. TE_0 optical power transmission from the thin film EEL to the polymer waveguide.

longer than 3 μm, the rate of the decrease in coupling efficiency is sub-exponential.

When the laser is embedded in the waveguide (gap = 0 μm), the facet reflectivity of the laser is degraded because the semiconductor/air interface changed to a semiconductor/polymer interface. A theoretical analysis of the laser with the output facet embedded in the waveguide resulted in the reflection of that facet decreasing to 13%.

To investigate the effect of thin film EEL active layer position on the coupling efficiency, 3 different active layer positions measured from the bottom of the polymer waveguide: X = 0.285 μm, 1.5 μm, and 2.715 μm are theoretically analyzed, as shown in Fig. 29(b). In Fig. 29(b), the thin film EELs are bonded to contact pads on the p contact side (X = 0.285 μm) and on the n contact side (X = 2.715 μm), respectively. Both cases are compared with the case in which the field launch position is at the center of the polymer waveguide. There are 100 calculated data points for both cases, X = 0.285 μm and X = 1.5 μm. For example, for the case of X = 0.285 μm, the coupling efficiencies are calculated as 0.7543, 0.3918, 0.3427, 0.2938, and 0.2771 for the gap distances 0 μm, 3 μm, 5 μm, 8 μm, and 10 μm, respectively. When the position of the active layer moves toward the center of the polymer waveguide, at X = 1.5 μm, the coupling efficiencies are calculated as 0.873, 0.42, 0.362, 0.2879, and 0.2615 for the gap distance 0 μm, 3 μm, 5 μm, 8 μm, and 10 μm, respectively.

In order to incorporate realistic factors, the effect of the angle of the entrance waveguide facet is not necessarily 90º, as shown in Fig. 30. The slope profile of the waveguide entrance facet, θ, depends on the processing conditions, such as the amount of time to cure the BCB polymer. The gap distance, d, is measured from the output facet of

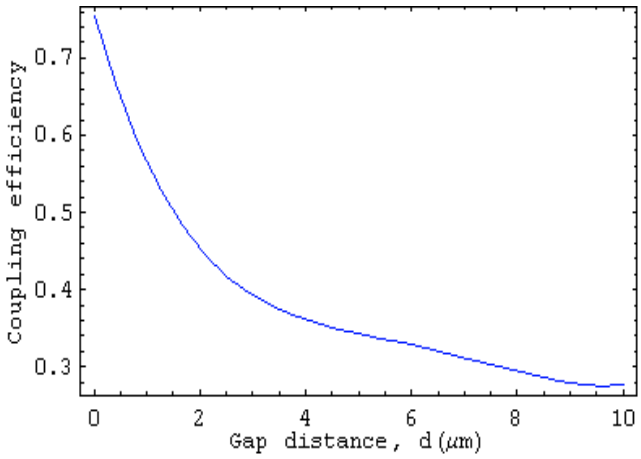

(a)

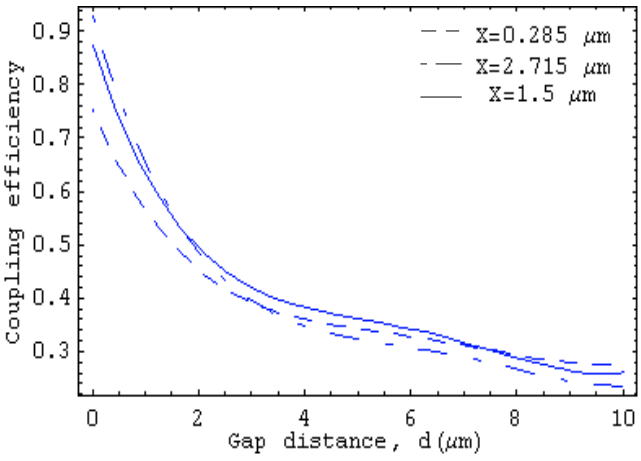

(b)

Figure 29. (a) Coupling efficiency as a function of the gap length, d, with X = 2.715 μm; (b) Coupling efficiency for for X = 0.285 μm, 2.715 μm, and 1.5 μm, respectively.

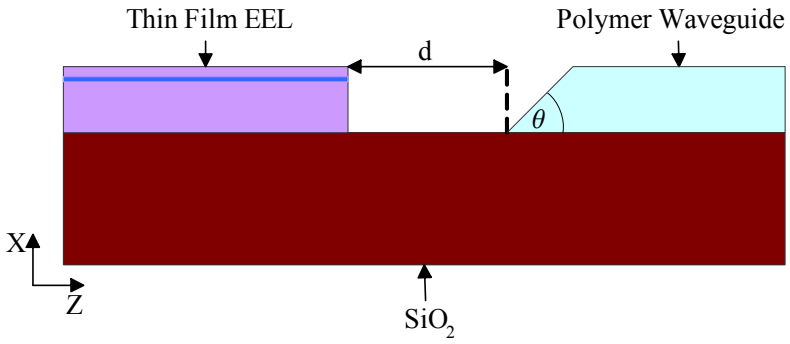

Figure 30. The waveguide entrance facet with angle θ.

the semiconductor waveguide to the starting point of the polymer waveguide entrance facet. The coupling efficiency is analyzed as a function of slope angles θ from 15º to 90º.

The simulation result of the optical power distribution in the XZ plane is shown in Fig. 31. In Fig. 31, the optical wave transmits from the thin film EEL to the BCB waveguide with entrance facet angle θ = 60º and field launch position X= 2.715 µm. The thickness of the polymer waveguide and the gap distance from the laser to the edge of the waveguide are 5 µm.

The coupling efficiency for an entrance angle of 60º is analyzed as a function of the gap distance, d, as shown in Fig. 31(a). The coupling efficiency decreases as the gap distance d increases. Figure 31(b) shows the coupling efficiency as a function of entrance angle θ with 5 µm separation between the laser and the starting point of the polymer waveguide. The coupling increases as the angle θ increases.

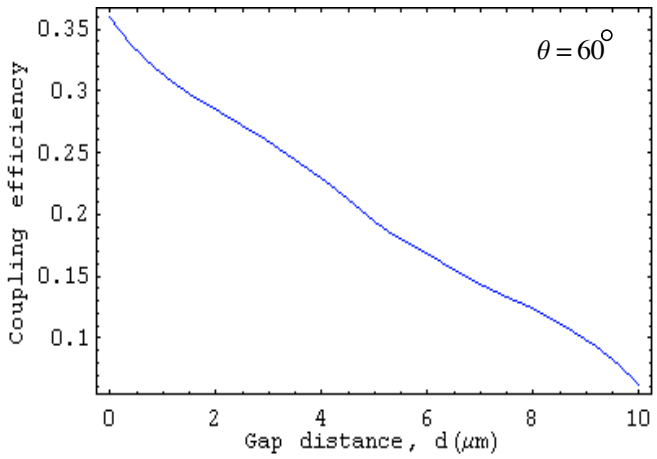

(a)

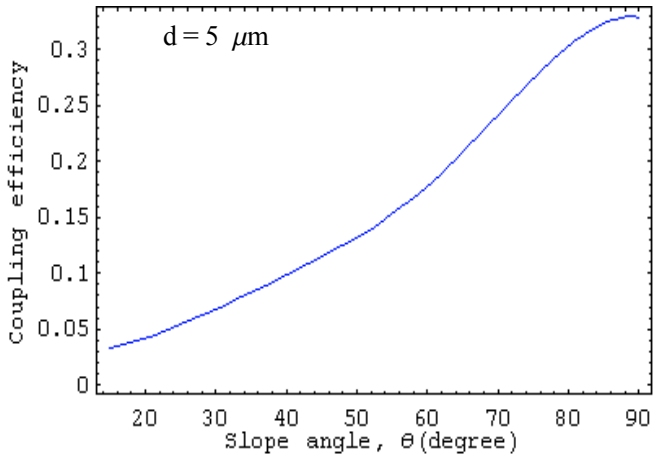

(b)

Figure 31. (a) The coupling efficiency as a function of gap length with entrance angle 60º; (b) The coupling efficiency as a function of slope angle, θ, with 5 μm separation.

4.4 Output Power and Threshold Current of InGaAsP/InP MQW Lasers

In order to characterize the performance of the fabricated laser structure, both the slope efficiency and the threshold current of the laser were simulated using Silvaco. The parameters used for the laser simulation are as follows [39]: In InP material, electron mobility is 2400 cm^2/Vs and hole mobility is 80 cm^2/Vs. In InGaAsP material, electron mobility is 4600 cm^2/Vs and hole mobility is 150 cm^2/Vs. The fraction of the energy band gap difference going to the conduction band is 60% at the InP-InGaAsP heterojunction. The radiative recombination time is 1.5×10^{-10} s. The carrier lifetime is 2.0×10^{-9} s. The contact stripe is 20 μm and the cavity length is 400 μm. The MQW gain model is employed in the simulation.

Figure 32(a) presents the simulated L-I curve of thin film EELs. The threshold current is calculated to be 20.9 mA. The threshold current was 30 mA experimentally. At an input current of 26.5 mA, the theoretical output power is 1 mW and the slope efficiency is calculated to be 18.4%. The slope efficiency is measure to be 2% experimentally. The error between the theoretical estimation and experimental results is caused by the increase in junction temperature from thermal heating. Figure 32(b) shows the threshold current, I_{th}, as a function of cavity length, L. The threshold current of the thin film EEL decreases with increasing cavity length.

In an effort to understand the effect of the thin film laser facet reflectivity on the threshold current, simulations were performed with varied mirror reflectivity, R. The cavity length of the laser was kept at 400 μm. The mirror reflectivity, R, is defined as the product of the front facet reflectivity, R_1, and the rear facet reflectivity, R_2. As shown in

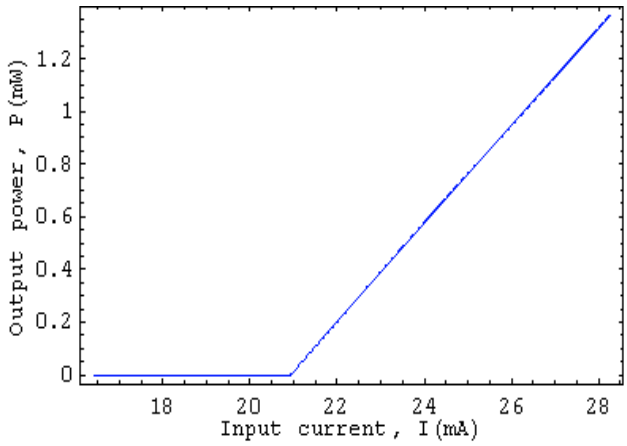

(a)

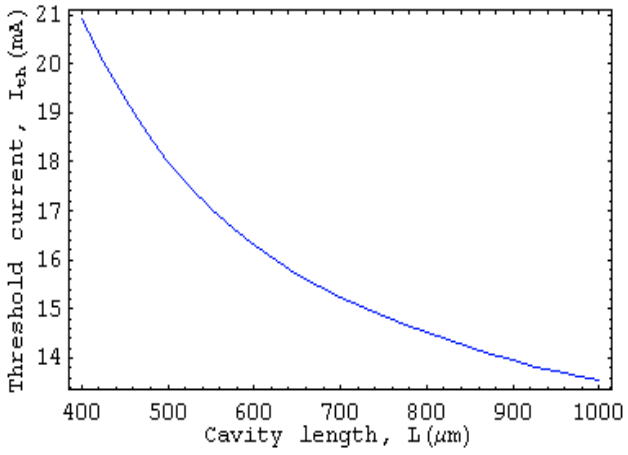

(b)

Figure 32. (a) L-I curve of the thin film EEL with cavity length 400 μm; (b) Threshold current of the thin film EEL, I_{th}, as a function of cavity length, L.

Fig. 33(a), the threshold current of the thin film EEL decreases with increasing mirror reflectivity. Figure 33(b) shows the slope efficiency analyzed as a function of the mirror reflectivity, R. For the case R_1 = 28% and R_2 = 28%, the slope efficiency is calculated to be 18.4%. However, for the cases R_1= 13% and R_2= 28% (one laser facet embedded in the polymer waveguide), the laser does not lase.

4.5 Laser to Waveguide Coupling as a Function of Laser to Waveguide Separation: Theory vs Experimental Estimates

The objective of this section is to compare theory to experiment for thin film lasers coupled to waveguides. In order to compare the output power measured experimentally to the coupling efficiency (defined in Section 4.3), the coupling loss from the waveguide to the photodetector and the propagation loss in the BCB waveguide have to be estimated. The coupling loss term is given by [77]

$$Loss = -10 \times \left(\mathrm{Log}_{10}\left[1 - \left(\frac{n_{wg} - n_{air}}{n_{wg} + n_{air}}\right)^2\right] + \mathrm{Log}_{10}\left[1 - \left(\frac{n_{detector} - n_{air}}{n_{detector} + n_{air}}\right)^2\right]\right) \tag{28}$$

where n_{wg} is the refractive index in the polymer waveguide, n_{air} is the refractive index in vaccum, and $n_{detector}$ is the refractive index of the detector surface. The loss is calculated as 1.8 dB from the waveguide to the photodetector. The propagation loss of the BCB waveguide is estimated using the direct cut back waveguide loss measurement method [78]. The principle of the method is the measurement of the waveguide output power on the same sample for different waveguide length. The propagation loss per unit length, α, can be expressed as Eq. 29.

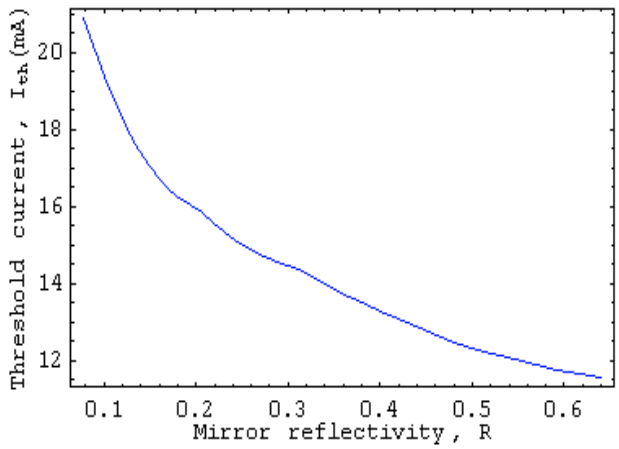

(a)

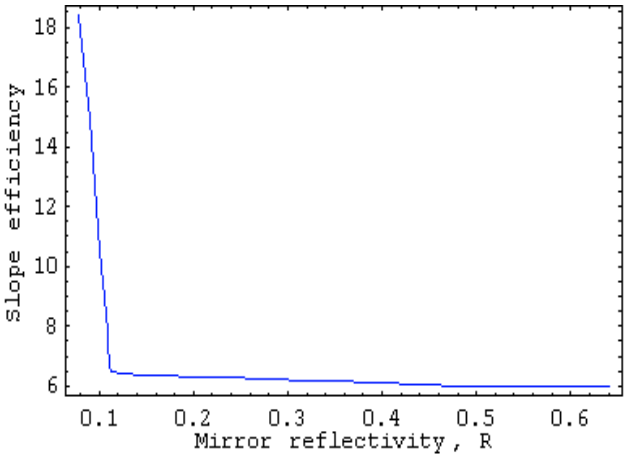

(b)

Figure 33. (a) Threshold current, I_{th}, as a function of mirror reflectivity, *R*; (b) Slope efficiency as a function of mirror reflectivity, *R*.

$$\alpha = -\frac{(Ln P_1 - Ln P_2)}{(L_1 - L_2)} \tag{29}$$

where P_1 and P_2 are waveguide output power measured with respect to waveguide length L_1 and L_2. The measured propagation loss is given in Table 8. For example, the

Table 8. CYCLOTENE BCB 3022-46 waveguide propagation loss measurements.

	Length L_1 (cm)	Length L_2 (cm)	Output Power P_1 (mW)	Output Power P_2 (mW)	Propagation Loss α (dB/cm)
1	0.48	0.24	0.0174	0.018	0.6
2	0.89	0.37	0.0079	0.00858	0.65

waveguide output power from the sample with gap distance 8 μm and waveguide length 4.8 mm is measured as 0.0174 mW. The output power from the same waveguide with length 2.4 mm is measured as 0.018 mW. Thus, by using Eq. 29, the propagation loss is calculated as 0.6 dB/cm. In this research, the average propagation loss constant, 0.625, is adapted. The BCB waveguide length were 2.8 mm, 3.9 mm, 2.4mm, and 3.7 mm for the 3 μm, 5 μm, 8 μm, and 10 μm, corresponding to the estimated waveguide absorption loss, 0.175 dB, 0.244 dB, 0.15 dB, and 0.231 dB, respectively.

The comparison of the waveguide output power as a function of laser to waveguide separation obtained by theoretical calculation to that estimated from the experimental results is shown in Fig. 34. There are 100 theoretical points, connected by a line, and 4 measured data points. The errors between the theoretical estimation and the experimental results in Fig. 34 are caused by several factors, such as the waveguide end facet quality and the waveguide entrance facet quality. In addition, the alignment problem introduced by the variation of the photodetector position to collect the optical power in the different

experiments is another factor contributing to the error. The errors for the separation of 3 μm 5 μm, 8 μm, and 10 μm are estimated to be 4%, 8.35%, 7.05%, and 8.29%, respectively.

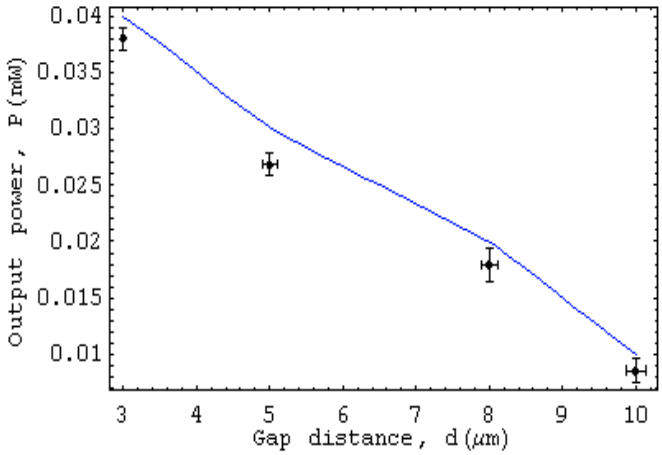

Figure 34. Comparison of waveguide output power calculated theoretically to that estimated experimentally.

4.1 Summary and Discussion

The present chapter discusses the theoretical simulation of the integration structure and comparison of theory to experiment. The slope efficiency, optical output power, and threshold current of the thin film EEL are also investigated toward optimization of fully embedded thin film lasers into polymer waveguides. The optical modes in the semiconductor laser cavity and in the polymer waveguide are analyzed using the thin film transfer matrix method. Only the fundamental mode exists in the semiconductor waveguide. There are three optical modes in the polymer waveguides. Thus, it is expected that most of the coupling occurs between the fundamental mode in the semiconductor waveguide and the fundamental mode in the polymer waveguide. In an effort to analyze the coupling efficiency, the coupling from the thin film laser to the waveguide decreases with increasing gap distance. By changing the field launch position

in the X direction, the coupling efficiency is estimated for two cases: p contact side bonded and n contact side bonded to the host substrate pads. The simulation shows that the coupling efficiency for the n contact side bonded to pads is higher than that for the p contact side bonded to pads. With the incorporation of the waveguide entrance angle θ into the simulation, higher coupling efficiency occurs for larger angle θ due to the larger effective area. Finally, the calculated waveguide output power as a function of gap distance is compared to the measured waveguide output power.

CHAPTER 5

CONCLUSIONS AND FUTURE RESEARCH

The design and fabrication methods of thin film EELs in this dissertation are contributions to the field of embedded optical interconnections. This dissertation reports the first demonstration of a thin film (microns thick) heterogeneously integrated EEL bonded to a Si host substrate. Processes for integrating these thin film lasers with BCB polymer waveguides have also been developed and tested, toward the implementation of embedded edge emitting sources in planar lightwave circuits. The key contributions made in this dissertation are summarized in this chapter. Future research directions are discussed in Section 5.2.

5.1 Summary of the Results

5.1.1 Design and Fabrication of Thin Film EELs

In this dissertation, thin film MQW InGaAsP/InP EELs have been fabricated using the WFC method. The laser structure and the processing techniques are presented. The lasers have been bonded to Si substrates and tested at room temperature. A threshold current of 30 mA has been demonstrated for a 20 μm p-contact stripe laser. The thickness of the final laser devices is around 5 μm. These are the first reported thin film MQW InGaAsP/InP EELs. These techniques enable the integration of thin film InGaAsP/InP lasers with electronic host substrates.

5.1.2 Integration and Test of Thin Film EELs with BCB Waveguides

The fabrication and integration of a thin film edge emitting laser (EEL) whose optical output is coupled into a polymer waveguide integrated on the same electrical interconnection substrate is reported in this dissertation research. The heterogeneous

integration of this InGaAsP EEL with a polymer waveguide structure is a fundamental building block toward the realization of planar lightwave circuits in an embedded optical interconnection format. The demonstration of a thin film laser embedded in a waveguide eliminates the need for either an external optical source coupled to the waveguide or a bump bonded optical source with a beam turning element to launch an optical wave into the waveguide. The laser threshold current is 30 mA, and the output approximated a Gaussian. The output of the waveguide is also measured, indicating that the laser lased and coupled to the polymer waveguide. The waveguide propagated the optical beam successfully. This is the first demonstration of a thin film EEL integrated with a polymer waveguide.

5.1.3 Comparison of Theory and Experiment

A compact and efficient numerical method, the thin film transfer matrix method, has been presented for the analysis of the optical modes in the semiconductor cavity. The coupling efficiency from the thin film laser to the polymer waveguide is analyzed using FEMLAB and the results are presented with the inclusion of different field launch positions and waveguide entrance angles.

5.2 Future Research

The developments in this dissertation are attempts made to simplify the system design of fully embedded optical interconnection. The scope of future contributions in the field of photonic lightwave circuits is very wide. Many aspects of thin film laser devices and their integration structure need to be optimized for higher levels of integration with multiple optoelectronic input and output for high data rate signal distribution and optical signal processing. On the most fundamental level, refinements of the theoretical models

need to be further investigated for predicting thin film laser performance, such as threshold current, output power, and heat dissipation.

There is a need for further investigation into the improvement of the temperature dependence of thin film InGaAsP lasers. Current injection results in heating, which in turn increases the temperature of the active region. The output power from the thin film laser gradually decreases, threshold current increases, and the slope efficiency decreases due to the temperature in the active layer increases. Heatsinks should be used to dissipate the heat from the active layer for higher performance of thin film laser devices, such as copper, silicon carbide (SiC), or silicon. The second approach to improving the temperature dependence of InGaAsP laser would be the use of new material systems, such as InGaAsN and InGaAlAs. Higher temperature operation has been anticipated in these material systems due to better electron and hole confinement as a result of increased band offsets and a more favorable band-offset ratio [79, 80].

The research developed in this dissertation is based on thin film gain-guided lasers. The phenomenon usually observed in gain-guided laser is spatial hole-burning [81] since the lateral transverse mode is controlled by carrier injection. This confinement is not stable, which results in a kink on the current-light output characteristics. In order to stabilize the transverse mode in the laser cavity, an index-guided laser could be used to improve the optical confinement and the stimulated emission process. One of the examples for index-guided lasers is the ridge waveguide laser. In the ridge waveguide structure, the use of a dielectric around the ridge inhibits current spreading in the *p*-InP layer [82]. The planar active layer of ridge waveguide lasers extends beyond the ridge. A fraction of the lasing mode overlaps with the dielectric, which has a considerably lower refractive index than that of the InP cladding layer. This overlap introduces an effective

lateral index step. The lateral index step is determined by the thickness of the waveguide layer.

In order to realize the thin film laser fully embedded inside the polymer waveguide, the rear facet of the thin film laser has to be coated with a high reflectivity dielectric to compensate for the photon loss from the front laser facet inside the waveguide. Multilayer dielectric mirrors can be conformally deposited by PECVD onto the laser facet [83]. The dielectric mirror could be composed of periods of alternating $\lambda/4$ layers of Si_3N_4 and SiO_2.

Another important refinement of the thin film EEL is its relaxation frequency, which fixes the limit of the modulation bandwidth for high data rate applications in optical interconnections. Several methods could be used to increase the relaxation frequency and extend the modulation bandwidth: (1) increasing the photon density within the laser cavity; (2) decreasing the photon lifetime; and (3) increasing the differential gain. The photon density can be increased by increasing the injected current. Photon lifetime can be reduced by shortening the optical cavity. The use of a strained quantum well structure in the active layer is another effective way to increase the differential gain.

REFERENCES

[1] E. D. Kyriakis-Bitzaros, N. Haralabidis, M. Lagadas, A. Georgakilas, Y. Moisiadis, and G. Halkias, "Realistic End-to-End Simulation of the Optoelectronic Links and Comparison with the Electrical Interconnections for System-on-Chip Applications," *IEEE J. Light. Technol.*, vol.19, pp.1532-1542, Oct. 2001.

[2] W. Ryu, J. Lee, H. Kim, S. Ahn, N. Kim, B. Choi, D. Kam, and J. Kim, "RF Interconnect for Multi-Gbit/s Board-Level Clock Distribution," *IEEE Trans. Adv. Packaging*, vol.23, pp.398-407, Aug. 2000.

[3] David A. B. Miller, "Physical Reasons for Optical Interconnection," *Int. J. Optoelectron.*, vol.11, pp.155-168, May/June 1997.

[4] S. K. Tewksbury and L. A. Hornak, "Optical Clock Distribution in Electronic Systems," *J. VLSI Signal Processing Systems for Signal, Image, and Video Technol.*, vol.16, pp.225-246, June/July 1997.

[5] M. Rassaian and M. W. Beranek, "Quantitative Characterization of 96.5Sn3.5Ag and 80Au20Sn Optical Fiber Solder Bond Joints on Silicon Micro-Optical Bench Substrates," *IEEE Trans. Adv. Packaging*, vol.22, pp.86-93, Feb. 1999.

[6] S. J. Walker and J. Jahns, "Optical Clock Distribution Using Integrated Free-Space Optics," *Opt. Comm.,* vol.90, pp.359-371, June 1992.

[7] P. J. Delfyett, D. H. Hartman, and S. Z. Ahmad, "Optical Clock Distribution Using a Mode-Locked Semiconductor Laser-Diode System," *IEEE J. Light. Technol.*, vol.9, pp.1646-1649, Dec. 1991.

[8] Y. Liu; L. Lin; C. Choi; B. Bihari; and R. T. Chen, "Optoelectronic Integration of Polymer Waveguide Array and Metal-Semiconductor-Metal Photodetector through Micromirror Couplers," *IEEE Photon. Technol. Lett*., vol.13, pp.355-357, Apr. 2001.

[9] S. Y. Cho, N. M. Jokerst, and M. Brook, "Comparison of Evanescent and Directly Coupled Optical Interconnection into Electrical Interconnection Substrate," *IEEE Proc. Lasaer and Electro-Optics Society Annu. Meeting,* vol.2, Nov. 2002.

[10] T. Suzuki, N. Ogawa, T. Nonaka, S. Y. Cho, S. W. Seo and N. M. Jokerst, "Embedded Optical Interconnections in Printed Wiring Board," *IEEE Proc. the 54th Electronic Components and Technology Conference*, June 2004.

[11] Y. Ishii, H. Tsuyoshi, H. Takahara, "Demonstration of on-PCB Optical Interconnection Using Surface-Mount Package and Polymer Waveguide," *IEEE Proc. the 53rd Electronic Components and Technology Conference,* May 2004.

[12] H. Shimizu, C. Setiagung, M. Ariga, Y. Ikenaga, K. Kummada, T. Hama, N. Ueda, N. Iwai, and A. Kasukawa, "1.3-μm-Range GaInNAsSb-GaAs VCSELs," *IEEE J. Select. Topics in Quantum Electron.*, vol.9, pp.1214-1219, Sep./Oct. 2003.

[13] A. Yue, K. Shen, R. Wang, and J. Shi, "Low Threshold Current 1.3-μm GaInNAs VCSELs Grown by MOVPE," *IEEE Photon. Technol. Lett.*, vol.16, pp.717-719, Mar. 2004.

[14] D. Sun, W. Fan, P. Kner, J. Boucart, T. Kageyama, R. Pathak, D. Zhang, and W. Yuen, "Sub-mA Threshold 1.5-μm VCSELs with Epitaxial and Dielectric DBR Mirrors," *IEEE Photon. Technol. Lett.*, vol.15, pp.1677-1679, Dec. 2003.

[15] Y. Yamada, H. Terui, Y. Ohmori, M. Yamada, A. Himeno, and M. Kobayashi, "Hybrid-Integrated 4×4 Optical Gate Matrix Switch Using Silica-Based Optical Waveguides and LD Array Chips," *IEEE J. Light. Technol.*, vol.10, pp.383-390, Mar. 1992.

[16] E. E. L. Friedrich, M. G. Oberg, B. Broberg, S. NIlsson, and S. Valette, "Hybrid Integration of semiconductor Lasers with Si-Based Single-Mode Ridge Waveguides," *IEEE J. Light. Technol.*, vol.10, pp.336-340, Mar. 1992.

[17] M. Kagami, A. Kawasaki, and H. Ito, "A polymer Optical Waveguide with out-of-Plane Branching Mirrors for Surface-Normal Optical Interconnections," *IEEE J. Light. Technol.*, vol.19, pp.1949-1955, Dec. 2001.

[18] S. Lehmacher and A. Neyer, "Integration of Polymer Optical Waveguides into Printed Circuit Boards," *IEE Electron. Lett.*, vol. 36, pp.1052-1053, June 2000.

[19] N. Bouadma and J. Semo, "1.3-μm GaInAsP/InP Buried-Ridge-Structure Laser and its Monolithic Integration with Photodetector Using Reactive Ion Beam Etching," *IEEE J. Light. Technol.*, vol.12, pp.742-748, May 1994.

[20] H. Yang, M. Nesnidal, A. Al-Muhanna, L. J. Mawst, D. Botez, T. A. Vang, F. D. Alvarez, and R. Johnson, "High-Power Single-Mode Simplified Antiresonant Reflecting Optical Waveguide (S-ARROW) Distributed Feedback Semiconductor Lasers," *IEEE Photon. Technol. Lett.*, vol.10, pp.1079-1081, Aug. 1998.

[21] M. Suzuki, Y. Tanaka, S. Akiba, Y. Kushiro, and H. Isshiki, "Monolithic Integration of InGaAsP/InP Distributed Feedback Laser and Electroabsorption Modulator by Vapor Phase Epitaxy," *IEEE J. Light. Technol.*, vol.LT-5, pp.1277-1285, Sep. 1987.

[22] H. Soda, M. Furutsu, K. Sato, N. Okazaki, Y. Yamazaki, H. Nishimoto, and H. Ishikawa, "High Power and High-Speed Semi-Insulting BH Structure Monolithic Electroabsorption Modulation/DFB Laser Light Source," *IEE Electron. Lett.,* vol. 26, pp.9-10, Jan. 1990.

[23] K. Y. Liou,, U. Koren, E. C. Burrows, M. Young, M. J. R. Martyak, M. Oron, and G. Raybon, "Y-Junction Power Divider in InGaAsP-InP Photonic Integrated Circuits," *IEEE J. Quantum Electron.*, vol.26, pp.1376-1383, Aug. 1990.

[24] W. K. Burns and A. F. Milton, "Mode Conversion in Planar-Dielectric Separating Wavguide," *IEEE J. Quantum Electron.*, vol.QE-11, pp.32-39, Aug. 1975.

[25] J. M. Verdiell, T. L. Koch, B. I. Miller, M. G. Young, U. Koren, F. Storz, and K. F. Brown-Goebeler, "A WDM Receiver Photonic Integrated Circuit with Net On-Chip Gain," *IEEE Photon. Technol. Lett.*, vol.6, pp.960-962, Aug. 1994.

[26] J. B. D. Soole, A. Scherer, H. P. Leblanc, N. C. Andreadakis, R. Bhat, and M. A. Koza, "Monolithic InP/InGaAsP/InP Grating Spectrometer for the 1.48-1.56 μm Wavelength Range," *Appl. Phys. Lett.,* vol.58, pp.1949-1951, May 1991.

[27] F. Xia, J. Wei, V. Menon, and S. R. Forrest, "Monolithic Integration of a Semiconductor Optical Amplifier and a High Bandwidth p-i-n Photodiode Using Asymmetric Twin-Waveguide Technology," *IEEE Photon. Technol. Lett.*, vol.15, pp.452-454, Mar. 2003.

[28] D. L. Veasey and D. R. Larson, "Integrated Optical Polarization-Discriminating Receiver in Glass," *IEEE J. Light. Technol.*, vol.13, pp.2244-2249, Nov. 1995.

[29] X. Yan, M. L. Masanovic, E. J. Skogen, Z. Hu, D. J. BLumenthal, and L. A. Coldren, "Optical Mode Converter Integration with InP-InGaAsP Active and Pssive Waveguides Using a Single Regrowth Process," *IEEE Photon. Technol. Lett.*, vol.14, pp.1249-1251, Sep. 2002.

[30] B. Mersali, A. Ramdane, and Carenco, "Optical-Mode Transformer: a III-V Circuit Integration Enabler," *IEEE J. Select. Topics in Quantum Electron.*, vol.3, pp.1321-1331, Dec. 1997.

[31] C. Tocci and H. J. Caulfield, *Optical Interconnection Foundations and Applications*, Artech House, Boston, 1994.

[32] G. Kim, X. Han, and R.T. Chen, "An 8-Gb/s optical backplane bus based on microchannel interconnects: design, fabrication, and performance measurements," *IEEE J. Light. Technol.*, vol.18, no.11, pp.1477-1486, Nov. 2000.

[33] R. T. Chen, L. Lin, C. Choi, Y. J. Liu, B. Bihari, L. Wu, S. Tang, R. Wickman, B. Picor, M. K. Hibbs-Brenner, J. Bristal, and Y. S. Liu, "Fully embedded Board-Level Guided-Wave Optoelectronic Interconnects," *Proc. IEEE,* vol.88, no.6, pp.780-793, June 2000.

[34] D. V. Plant, M. B. Venditti, E. Laprise, J. Faucher, K. Razavi, M. Chateauneuf, An. G. Kirk, and J. S. Ahearn, "256-Channel Bidirectional Optical Interconnect Using VCSELs and Photodiodes on CMOS," *IEEE J. Light. Technol.*, vol.19, no.8, pp.1093-1103, Aug. 2001.

[35] S. Y. Cho, S. W. Seo, M. A. Brooke, and N. M. Jokerst, "Integrated Detectors for Embedded Opticl Interconnections On Electrical Boards, Modules, and Integrated Circuits," *IEEE J. Select. Topics in Quantum Electron.*, vol.8, pp.1427-1434, Nov./Dec. 2002.

[36] H. Wada, "1.3μm InP/InGaAsP Lasers Fabricated on Si Substrates by Wafer Bonding," *IEEE J. Select. Topics in Quantum Electron.*, vol.3, no.3, pp.937-942, June 1997.

[37] J. C. Fan, K. Y. Chen,G. Lin, C. P. Lee, "Stripe-Geometry GaAs-InGaAs Laser Diode with Back-Side Contact on Silicon by Epitaxial Lift-Off," *IEE Electron. Lett.*, pp. 1095-1096, vol. 33, June 1997.

[38] Pollentier, L. Buydens, P. Van Daele, and P. Demeester, "Fabrication of a GaAs-AlGaAs GRIN-SCH SQW Laser Diode on Silicon by Epitaxial Lift-Off," *IEEE Photon. Technol. Lett.*, vol.3, no.2, pp.115-117, Feb. 1991.

[39] S. L. Chuang, *Physics of Optoelectronic Devices*, Wiley, New York, 1995.

[40] W. Streifer, D. R. Scifres, and R. D. Burnham, "Analysis of Gain-Induced Waveguiding in Stripe-Geometry Diode Lasers," *IEEE J. Quantum Electron*., vol.QE-14, pp.418-427, June 1978.

[41] W. T. Tsang, "The Effects of Lateral Current Spreading, Carrier Out-Diffusion, and Optical Mode Losses on the Threshold Current Density of GaAs-AlxGa1-xAs Strip-Geometry DH Lasers," *J. Appl. Phys.*, vol.49, pp.1031-1044, Mar. 1978.

[42] B. W. Hakki, "Carrier and Gain Spatial Profiles in GaAs Strip Geometry Lasers," *J. Appl. Phys.*, vol.44, pp.5021-5029, Nov. 1973.

[43] S. Sze, *Physics of Semiconductor Devices*, Wiley, New York, 1981.

[44] W. B. Joyce, "Current-Crowded Carrier Confinement in Double-Heterostructure Lasers," *J. Appl. Phys.*, vol.51, pp.2394-2401, May 1980.

[45] Nahory, R. E. and M. A. Pollack., "Threshold Dependence on Active-Layer Thickness in InGaAsP/InP D.H. Lasers," *IEE Electron. Lett.*, vol.14, pp.727-729, Nov. 1978.

[46] T. Ikegami, "Reflectivity at Facet and Oscillation Mode in Double–Heterostructure Injection Lasers," *IEEE J. Quantum Electron*., vol.8, pp.470-476, June 1972.

[47] W. T. Tsang, "Extremely Low Threshold AlGaAs Graded-Index Waveguide Separated Confinement Heterostructure Lasers Grown by Molecular Beam Epitaxial," *Appl. Phys. Lett.*, vol. 53, pp88-90, Feb. 1982.

[48] N. K. Dutta, "Gain-Current Relation for In/sub 0.72/Ga/sub 0.28/As/sub 0.6/P/sub 0.4/ Lasers," *J. Appl. Phys.* vol.52, pp.55-60, Jan. 1981.

[49] R. J. Nicholas, J. C. Portal, C. Houlbert, P. Perrier, and T. P. Pearsall, "An Experimental Determination of the Effective Masses for GaInAsP Alloys on InP," *Appl. Phys. Lett.*, vol.34, pp.492-494, Apr. 1979.

[50] Mitsuo Fukuda, *Optical Semiconductor Devices*, Wiley, New York, 1999.

[51] M. T. Bernius, David C. Burdeaux, C. C. Fulks, P. Garrou, R. H. Heistand, Jr., T.M. Stokich," Planarization with CYCLOTENE* 3022 (BCB) Polymer Coatings," *Proc. MRS*, vol. 308, p. 517, 1993.

[52] D. W. Castillo, P. Garrou, R. H. Heistand, C. E. Mohler, M. R. Stachowiak, A. J. G. Strandjord, and T. G. Tessier, "Micro-ATR-IR As A Probe of BCB Layers For MCM-D/L Applications," *Proc MRS*, vol.323, pp.295, 1993.

[53] S. A. B. Allen, N. R. Grove, T. C. Hodge, P. Kohl, and B. Sinno, "Thermo-Mechanical Stresses in Spin-Cast Polymer Films on Silicon Substrates," *Int. J. Microcircuits Electron. Packaging*, vol.20, pp.12-20, 1997.

[54] A. Chakrabarti, J. Curphy, S. Froelicher, D. Hawn, J. Hetzner, J. Im, C. Karas, G. Meyers, E. O. Shaffer, Jr., T.M. Stokich, and A. J. G. Strandjord, "On the Mechanical Reliability of photo-BCB," *Thin Film Dielectric Polymer for Microelectronic Applications Proceed. Workshop on Mechanical Reliability of Polymeric Materals and Plastic Packages of IC Devices*, vol.25, pp.191, 1998.

[55] G. Arvidsson, P. Eriksen, G. Gustafsson, J. Hagel, J. Hammar, P. Henriksson, and G. Palmskog, "Low Cost Single Mode Optical Passive Coupler Devices with an MT Interface Based on Polymeric Waveguides in BCB," *Int. J. Microcircuits and Electronic Packaging*, vol.21, pp.151, 1998.

[56] D. Marcuse, *Theory of Dielectric Optical Waveguides 2nd edition*, Academic, London, 1994.

[57] Y. Fu, N. Kok, and A. Bryan, "A Novel One Step Integration of Edge-emitting Laser Diode with Micro-Elliptical Lense Using Focused Ion Beam Direct Deposition," *IEEE Trans. Semiconduct. Manufact.*, vol.15, pp.2-8, Feb. 2002.

[58] T Yamada, T. Hashimoto, T. Ohyama, Y. Akahort, A. Kaneko, K. Kato, R. Kasaharo, and M. Ito, "New Planar Lightwave Circuit Platform Eliminating Si Terraces and Its Application to Opto-Electronic Hybrid Integrated Module," *IEICE Trans. Commun.*, vol.E84-B, pp.685-692, May 2001

.

[59] N. Yamanaka, K. Endo, K. Genda, H. Fukuda, T. Kishimoto, and S. Sasaki, "320Gb/s High-Speed ATM Switching System Hardware Technologies Based on Copper-Polyimide MCM," *IEEE Trans. Comp., Packaging, Manuf. Tech. Part B*, vol.18, pp.83-91, Feb. 1995.

[60] T. Sakamoto, H. Tsuda, M. Hikita, T. Kagawa, K. Tateno, and C. Amano, "Optical Interconnection Using VCSELs and Polymetric Waveguide Circuits," *IEEE J. Light. Technol.*, vol.18, pp.1487-1492, Nov. 2000.

[61] J. A. Kong, *Electromagnetic Wave Theory 2nd edition*, Wiley, New York, 1990.

[62] M. Koshiba, H. Saitoh, M. Eguchi, and K. Hirayama, "Simple Scalar Finite Element Approach to Optical Waveguides," *IEE Proc. J.*, vol.139, pp.166-171, Apr. 1992.

[63] M. Koshiba, *Optical Waveguide Theory by the Finite Element Method*, KTK Scientific and Kluwer Academic, Holland, 1992.

[64] O. C. Zienkiewitz, *The Finite Element Method*, 3rd ed., McGraw-Hill, New York, 1973.

[65] St. Kollakowski, A. Strittmatter, E. Dröge, E. H. Böttcher, and Bimberg, "65 GHz InGaAs/InAlGaAs/InP waveguide-integrated photodetectors for the 1.3-1.55 μm wavelength regime," *Appl. Phys. Lett.*, vol. 74, pp. 612-614, Jan. 1999.

[66] E. H. Böttcher, H. Pfitzenmaier, E. Dröge, S. Kollakkowski, A. Stittmatter, D. Bimberg, and R. Steingrüber "Distributed waveguide-integrated InGaAs MSM Photodetectors for high-efficiency and ultra-wideband operation," *IEEE 11th Intern. Conf. on Indium Phosphide and Related Mat. Proc.,* pp. 79-82, May 1999.

[67] R. T. Chen, L. Lin, C. C. Choi, Y. J. Liu, B. Bihari, L. Wu, S. Tang, R. Wickman, B. Picor, M. K. Hibbs-Brenner, J. Bristow, and Y. S. Liu, "Fully Embedded Board-Level Guided-Wave Optoelectronic Interconnects," *Proc. of the IEEE*, vol. 88, pp. 780-793, June 2000.

[68] C. H. Buchal, A. Roelofs, M. Siegert, and M. Löken, "Polymeric strip waveguides and their connection to very thin ultrafast metal-semiconductor-metal detectors," *Mat. Res. Soc. Symp. Proc.* vol. 597, pp. 97-102, Dec. 2000.

[69] F. Gouin, L. Robitaille, C. L. Callender, J. Noad, and C. Almeida, "A 4x4 optoelectronic switch matrix integrating an MSM array with polyimide optical waveguides," *Proc*. *SPIE,* vol.3290, pp.287-295, Jan. 1997.

[70] Y. Nakano and Y. Noguchi, "1.3 μm Buried-Heterostructure Lasers on p-type InP Substrates," *IEEE Quantum. Electron*., vol.21, pp.452-457, May 1985.

[71] I. F. Lealman, D. M. Cooper, S. D. Perrin, and M. J. Harlow, "Effect of Zn Doping on Differential Gain and Damping of 1.55 μm InGaAs/InGaAsP MQW lasers," *IEE Electron. Lett.*, vol.28, pp.1032-1034, May 1992.

[72] H. Sugiura, S. Kondo, M. Mitsuhara, S. Matsumoto, and M. Itoh, "Be-Zn Interdiffusion and its Influence on InGaAsP Lasers Fabricated by Hrbrid Growth of

Chemical Beam Epitaxial and Metalorganic Vapor Phase Epitaxy," *Appl. Phys. Lett.*, vol. 70, pp.2846-2848, May 1997.

[73] J. Strandberg, H. Thiede, A. Karlsson, P. Bodo, J. Haglund, S. Valizadeh, and A. Weiland, "Versatile Multilayer MCM-D Structure for High Reliability Applications," *IEEE Trans. Comp., Packaging, and Manufact. Technol.*, vol.20, pp.327-333, Aug. 1997.

[74] I. P. Kaminow, L. W. Stulz, J. S. KO, A. G. Dental, R. E. Nahory, J. C. Dewinter, and R. L. Hartman, "Low-Threshold InGaAsP Ridge Waveguide Lasers at 1.3 μm," *IEEE J Quantum Electron.*, vol.QE-19, pp.1312-1318, Aug. 1983.

[75] J. Kraus and P. P. Deimel, "Full-Width-Half-Maximum and Confinement of Optical Modes in Multiple-Quantum-Well Laser Structures," *IEEE J. Lightwave Technol.*, vol.11, pp.1802-1805, Nov. 1993.

[76] E. Anemogiannis, E. N. Glytsis, and T. K. Gaylord, "Efficient Solution of Eigenvalue Equations of Optical Waveguiding Structures," *IEEE J. Lightwave Technol.*, vol.12, pp.2080-2084, Dec. 1994.

[77] D. K. Cheng, *Field and Wave Electromagnetis 2nd edition*, Prentice-Hall, New Jersey, 1999.

[78] N. M. Jokerst, M. A. Brook, S. Y. Cho, S. Wilkinson, M. Vrazel, S. Fike, J. Tabler, Y. J. Joo, S. W. Soo, D. S. Wills, and A. Brown, "The Heterogeneous Integration of Optical Interconnection Into Integrated Microsystems," *IEEE J. Select. Topics in Quantum Electron.*, vol.9, pp.350-360, Apr. 2003.

[79] B. Chen, W. Wanf, X. J. Wang, J. Y. Zhang, and Z. Fan, "A Novel 1.3 μm High T_0 Al GaInAs/InP Strained Compensated Multi-Quantum Well Complex-Coupled Distributed Feedback Laser Diode," *Jpn. J. Appl. Phys.*, vol. 35, pp.5096-5100, Sep. 1999.

[80] M. Kondow, K. Uomi, A. Niwa, T. Kitatani, S. Watahiki, and Y. Yazawa, "GaInNAs: A Novel Material for Long Wavelength-Range Laser Diodes with Excellence High-Temperature Performances," *Jpn. J. Appl. Phys.*, vol. 35, pp.1273-1275, Feb. 1996.

[81] Y. Nishimura, "Spectral Hole-Burning and Nonlinear-Gain Decrease in a Band-to-Level Transition Semiconductor Laser," *IEEE Quantum Electron.*, vol.QE-9, pp.1011-1019, Oct. 1973.

[82] I. P. Kaminow, R. E. Nahory, M. A. Pollack, L. W. Stulz, and J. C. DeWinter, "Single-Mode C.W. Ridge-Waveguide Laser Emitting at 1.55 μm," *IEE Electron. Lett.,* vol.15, pp.763-765, Nov. 1979.

[83] S. C. Horst, D. S. Hinkel, J. L. Fitz, and H. Turk, "High-Reflectance Dielectric Mirrors Deposited by Plasma-Enhanced Chemical Vapor Deposition on GaAs-

AlGaAs Semiconductor Lasers with Inductively Coupled Plasma Etched Facets," *IEEE Photon. Technol. Lett.,* vol. 12, pp. 1325-1327, Oct. 2000.

VITA

Hung-Fei Kuo received the Bachelor of Science degree in Electrical Engineering from Feng Chia University, Taichun, Taiwan in 1992. He received the Master of Science degree in Electrical Engineering from Syracuse University, Syracuse, New York in 1998. His masters degree project involved the design and fabrication of semiconductor fiber amplifiers and fiber polarizers. He is a member of the Institute of Electrical and Electronics Engineers (IEEE).